communications biology

A Nature Portfolio journal

Article

https://doi.org/10.1038/s42003-025-09184-4

Optimal stochastic tracking control for brain network dynamics

Kangli Dong [1], Siya Chen [2,3] ✉, Ying Dan [4], Lu Zhang[5], Xinyi Li[1], Wei Liang[6], Yue Zhao[7] & Yu Sun [8]

Network control theory (NCT) has recently been utilized in neuroscience to facilitate our understanding of brain stimulation effects and explore optimal paradigms. This paper considers stochastic brain dynamics and introduces optimal stochastic tracking control to synchronize brain dynamics to target dynamics rather than to a target state at a specific time point. For all participants, we utilize a gradient descent optimization method to estimate the parameters (e.g., the coupled matrix and the variance matrix) for the brain network dynamical system. We then utilize optimal stochastic tracking control techniques to drive the original unhealthy dynamics by controlling a certain number of nodes to synchronize with target healthy dynamics. Results show that the tracking energy is negatively correlated with the average controllability of the brain network system, while the energy of the optimal state transfer control is significantly related to the target state value. For a 100-dimensional system, the dynamics over 90% of the nodes can be improved by controlling five nodes with the lowest tracking energy. These findings highlight the potential of stochastic tracking control as a promising approach for guiding brain stimulation interventions in the treatment of neurological disorders such as stroke.

The human brain functions as a complex and expansive network, with diverse parcellation templates delineating distinct regions according to anatomical or functional criteria. In addition to understanding the topological changes in brain networks under pathological conditions[1–9], brain stimulation interventions have emerged as a potential effective method for modulating brain networks and treating related disorders. In recent years, the clinical use of transcranial magnetic stimulation (TMS)[10] and transcranial direct current stimulation (tDCS)[11], two representative non-invasive brain stimulation (NIBS) techniques, has shown promising results, driven by advancements in non-invasive brain stimulation[12]. Theoretically, Network Control Theory (NCT) provides us with the opportunity to comprehend the impact of these stimulation effects on brain dynamics and, consequently, theoretically explore optimal stimulation paradigms. NCT posits that the human brain functions as a dynamic system, undergoing transitions through diverse activation patterns, or brain states, over time[13]. NCT quantifies brain network properties based on regional interactions and overall network dynamics, providing a computational framework to elucidate how functional brain dynamics originate from underlying network structures[14]. In the context of NCT, a brain network is considered controllable if it can be controlled/pushed into different active 'states'. These states are defined as coordinated neurophysiological activities across brain regions at specific moments[13]. Based on NCT, optimal brain network control exerts a particularly significant influence. In essence, it generates time-varying inputs that drive the brain network system to a target state. These inputs are designed to minimize the squared magnitude of the input signal integrated over time, referred to as the 'control energy', and as the distance from a target state, typically set to be equal to the target state or an $N \times 1$ zero vector for an N-dimension system. Optimal brain network control has been extensively studied to elucidate executive function and brain network development[15–17], epilepsy[18,19], schizophrenia[20], psychiatric disorders[21,22], and psychedelic research[23,24], etc. In this work, we introduce a framework of optimal tracking control for brain network dynamics, aiming to advance the existing framework of optimal transfer control in current research.

The rehabilitation of stroke and post-stroke aphasia (PSA) is an appropriate clinical scenario to be explained and guided by optimal brain network control. Stroke is a cerebral disorder caused by damage to cerebral blood vessels due to various factors, resulting in localized or widespread brain injury. As a significant cause of aphasia, stroke can impair language

[1]Department of Biomedical Engineering, College of Engineering, Shantou University, Shantou, Guangdong, China. [2]School of Computer Science and Technology, Dongguan University of Technology, Dongguan, Guangdong, China. [3]Department of Computer Science, City University of Hong Kong, Hong Kong, Hong Kong, China. [4]Department of Biomedical engineering, Chinese University of Hong Kong, Hong Kong, Hong Kong, China. [5]Department of Rehabilitation, Sir Run Run Shaw Hospital, Zhejiang University School of Medicine, Zhejiang University, Hangzhou, Zhejiang, China. [6]Department of Computer Science and Engineering, Lehigh University, Bethlehem, PA, USA. [7]Department of Urology, Xiang'an Hospital of Xiamen University, Xiamen University, Xiamen, Fujian, China. [8]Key Laboratory for Biomedical Engineering of Ministry of Education of China, Zhejiang University, Hangzhou, Zhejiang, China. ✉e-mail: chensiya@dgut.edu.cn

abilities, leading to communication difficulties due to acute brain damage[25,26]. The recovery process is complicated by both short-term and long-term speech impairments, as well as the diverse transitions observed across different forms of PSA[27]. Some individuals with chronic aphasia (lasting more than six months) can achieve significant improvements through speech therapy[28]. Although TMS (especially repetitive TMS, i.e., rTMS) and tDCS have been proven to be effective for stroke motor rehabilitation, the parameters of stimulation and clinical trial design characteristics remain to be clarified, and the mechanism of stimulation remains to be explored[29]. Both tDCS and rTMS have demonstrated potential in enhancing speech and language outcomes for stroke patients. However, prior to the implementation of NIBS in clinical practice, additional research is necessary to ascertain the optimal parameters, as well as the underlying mechanisms underlying their therapeutic effects[30].

Although optimal brain network control can provide potentially feasible theoretical guidance in the treatment of many diseases using NIBS techniques, the prevailing methodology exhibits certain limitations. Existing optimal brain network control methods are predominantly based on the assumption of simplest linear systems, i.e., $\dot{\mathbf{x}}(t) = \mathbf{A}\mathbf{x}(t) + \mathbf{B}\mathbf{u}(t)$. This framework is reasonable, as brain dynamics can be approximated by linear dynamics to some extent[31]. However, the current assumption still has overlooked two significant factors that cannot be ignored: First, the current assumption do not consider the spontaneous dynamics in brain networks. The current dynamical equations do not include a noise term, and the assumption cannot satisfy the condition that brain dynamics passively evolve according to their own dynamic inertia when uncontrolled. Secondly, the fundamental aspect of dynamics lies in time series. The current assumption posits a state as a distinct point in time within the dynamics, and the objective is to transition from one state to another. Dysfunctional brain dynamics can be observed in common clinical scenarios such as pain[32], epilepsy[33], small vessel disease[34], schizophrenia[35], and stroke[36]. Considering the intrinsic dynamics and conditional dependencies of brain activity, the brain continuously integrates, coordinates, and reacts to both internal and external stimuli over various time scales[37,38]. A single discrete state cannot capture the characteristics of brain dynamics, and merely pushing one state to another is insufficient.

In this investigation, we integrated the aforementioned factors into optimal brain network control, and introduced the concept of *optimal stochastic tracking control* to reevaluate the brain network control problem. The objective of optimal stochastic tracking control is to drive the original dynamics towards target dynamics, ensuring that their statistical properties are similar, which aligns more closely with the objective of achieving brain dynamic control. Furthermore, to achieve optimal stochastic tracking control in practical functional magnetic resonance imaging (fMRI) measurements, we developed and refined a gradient descent optimization method. This method enables the estimation of statistical variance and a diagonally symmetric connectivity matrix for the brain network system. Employing fMRI data from stroke and post-stroke aphasia cases as illustrative examples, we endeavored to drive the pathological dynamics towards healthy dynamics. By comparing the results with existing optimal control strategies (referred to as *optimal state transfer control* in subsequent sections), we validated that the proposed framework can reflect the intrinsic controllability characteristics of the brain network system. We also explored the minimum cost required to achieve an acceptable control effect, aiming to provide a basis for clinical brain stimulation paradigms.

Results

The research framework of this investigation can be found in Fig. 1. In this investigation, we present an investigation of introducing an optimal stochastic tracking control framework to brain network control, aiming to provide insights that can guide optimal brain stimulation interventions. In this section, we employ stroke and post-stroke aphasia as examples to illustrate the efficacy of the control strategy. We first performed controllability analysis for different spatial locations related to lesions. We then present the results of a representative participant to substantiate the efficacy of the optimal tracking control. We further investigate the spatial distribution characteristics of tracking energy and its relationship with the intrinsic controllability of brain network systems. Further, we attempt to select control nodes based on tracking energy to investigate how the dynamics of brain network systems can be controlled to the minimum extent. Finally, we provide the results of optimal state transfer control for comparison. We utilized a 100-ROI and a 400-ROI template from the Schaefer 2018 parcellation[39] for brain network modeling. Due to space constraints, part of the results for the 100-ROI brain network system and the correlation analysis of nodal metrics are available in the Supplementary Fig. S1 to Supplementary Fig. S15.

Controllability and FC changes for different spatial locations related to lesions

Using fMRI and DWI data from stroke and post-stroke aphasia cases as examples, we attempted to drive the pathological dynamics towards healthy dynamics. We used two open-source datasets: the Aphasia Recovery Cohort (ARC) Dataset and the Resting-state data of the Older Adults Dataset, which are described in Section 4. The ARC dataset comprises 148 post-stroke aphasia patients (including four aphasia types: Anomic, Broca, Conduction, and Global) and 26 normal stroke patients. The Older Adults dataset includes 28 healthy older participants.

We first conducted an analysis and comparison of controllability metrics based on the spatial information of the lesions for patients in the ARC dataset. Controllability quantifies the efficiency and potential of a specific brain region or node in driving state transitions across the entire network, as further described in Definition 3. We defined three lesion-related spatial regions: the perilesional area encompassing regions immediately surrounding the lesion, as well as the first and second anatomical neighbors adjacent to the perilesional region, as delineated using the Schaefer 400 ROI parcellation. Figure 2a illustrates the overlay of these regions. Subsequently, we conducted comparisons of modal and average controllability across these lesion zones within different resting-state networks. As shown in Fig. 2b, we can see that the rank value of average controllability decreased progressively with increasing distance from the lesion for all network groups. In contrast, the rank value of modal controllability increased with distance from the lesion. This means that regions farther from the lesion exhibit a higher ability to drive from the current state to a neighboring state, while regions closer to the lesion have a higher ability to drive from the current state to a distant, hard-to-reach state.

Further, we compared regions connected to the lesion versus non-connected regions. First, SC networks were constructed for each patient via fiber tracking on DWI images. Regions with non-zero SC to the lesion were defined as 'connected regions', whereas those with zero SC were 'non-connected regions'. We then compared two controllability metrics—average controllability and modal controllability—between two groups, as shown in Fig. 2c. It can be seen that connected regions exhibited larger average controllability rank values (lower rank), whereas non-connected regions had smaller average controllability rank values (higher rank). In contrast, modal controllability followed an opposite pattern. The results further substantiate that the changes in controllability after stroke are directly related to the lesions.

We then compared three groups: healthy controls in Resting-state for Older Adults Dataset, non-aphasic stroke, and aphasic stroke including 4 aphasia types: Anomic, Broca, Conduction, Global, for basic FC statistics, which were estimated via fisher-z transformed Pearson correlation on fMRI data. Three types of FC were analyzed: homotopic (interhemispheric homologous), ipsilesional (intra-lesion hemisphere), and contralesional (intra-non-lesion hemisphere). For each type, FC values were subjected to kernel density estimation (KDE) to characterize distributional differences across groups in Fig. 2d. For homotopic connections, both normal stroke and aphasia patients showed significantly reduced FC compared to healthy controls (FDR-corrected $p = 0.002$), which is consistent with previous research findings[40,41]. In contrast, ipsilesional FC was enhanced in normal stroke and aphasia patients compared with healthy controls (FDR-corrected

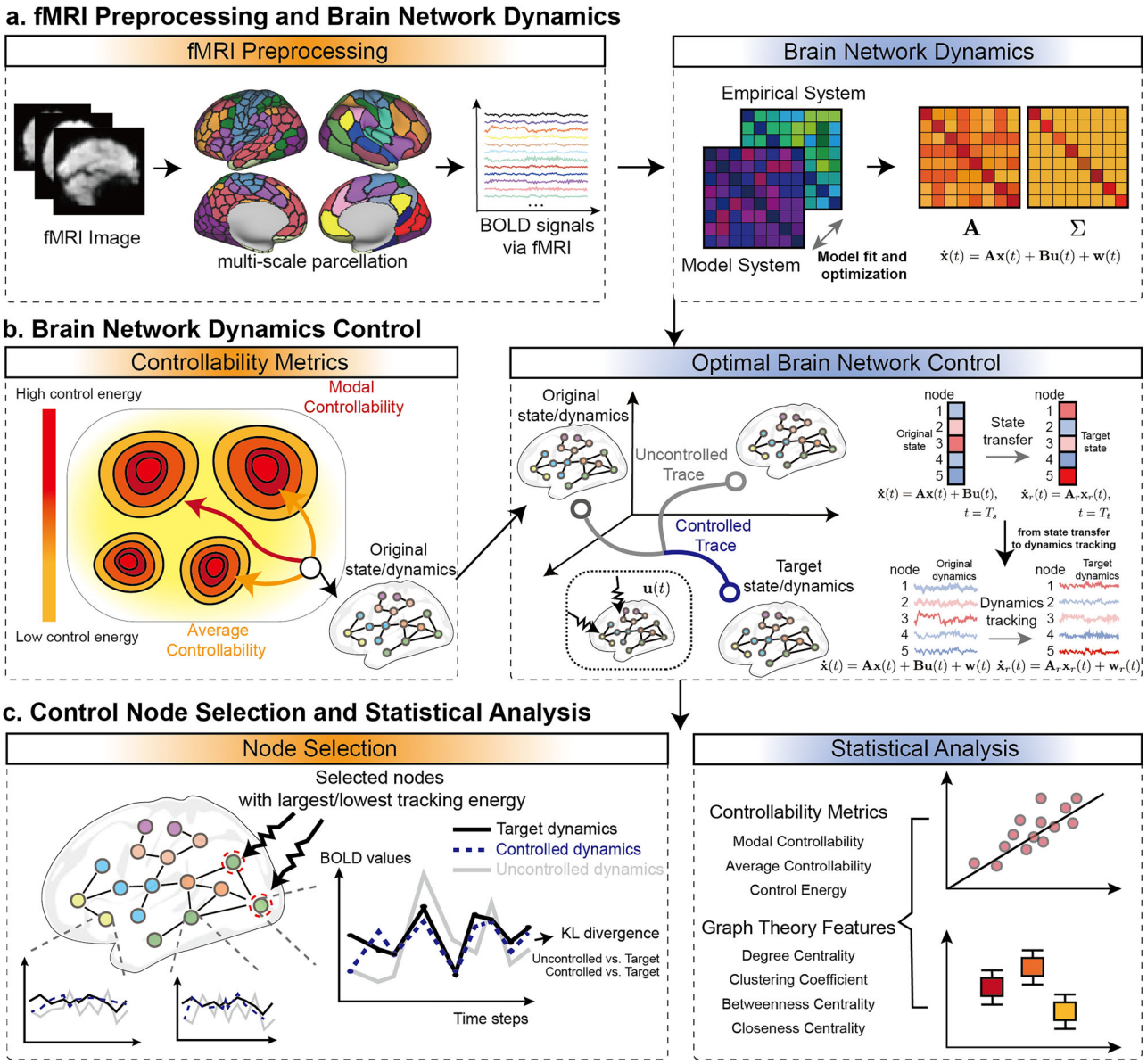

Fig. 1 | Framework. a fMRI Data Preprocessing and Brain Network Model Construction. The preprocessing phase includes fMRI denoising[88] and obtaining the BOLD signal after cortical parcellation. Here we utilized the 100-ROI and 400-ROI templates from Schaefer2018 parcellation[39], at different scales. In the brain network model construction phase, we employed the gradient descent optimization method to estimate the **A** and **Σ** of the network system, thereby making the network model closely approximate the fMRI dynamics. The coupled matrix **A** and variance matrix **Σ** were further used to carry out the optimal stochastic tracking control and optimal state transfer control. **b** Brain Network Control. First, we estimated the two intrinsic properties of brain network systems, namely average controllability and modal controllability, to explore the relationship between these properties and the optimal control characteristics. Second, as a prerequisite for optimal state transfer control and optimal stochastic tracking control, we extracted the original brain states and dynamics (i.e., time series) for each stroke and post-stroke aphasia patient, and extracted target brain states and dynamics from the healthy group as control targets. Finally, we executed two different optimal control strategies and examined the characteristics of their primary performance (i.e., control energy). **c** Control Node Selection and Statistical Analysis. We conducted statistical analyses on the control energy, the controllability of the brain network, and the nodal metrics under two optimal control strategies. Additionally, based on the control energy (i.e., the tracking energy of optimal stochastic tracking control), we attempted to explore the control effects using Kullback-Leibler (KL) divergence with different numbers of control nodes by incrementally adding control nodes.

$p < 0.001$), which possibly reflects compensatory reorganization[42]. No significant changes were found for contralesional FC.

Fitting model for brain network dynamic system

To better control brain network dynamics, rather than performing discrete state transfers, we first obtained the optimal parameters (the coupled matrix $\mathbf{A} \in \mathbb{R}^{N\times N}$ and the variance matrix $\mathbf{\Sigma} \in \mathbb{R}^{N\times N}$) for each participant's brain network system in the two datasets using gradient descent optimization, as illustrated in Fig. 3a, b, with the participant having ID 2121 used as an example. Since the optimization process involves two important hyperparameters (η_C and η_Σ) that need to be adjusted, we targeted two objectives: maximizing the average correlation and minimizing the model error/distance between the approximate dynamic model and the original fMRI data. The optimal hyperparameters were obtained through a simple grid search. We can observe the optimized **A** and **Σ** matrices in Fig. 3a, along with the corresponding optimization processes for 400-ROI brain networks in Fig. 3b. The optimal hyper-parameter setting for M2121's 400-ROI system, $\eta_C = 4 \times 10^{-5}$ and $\eta_\Sigma = 0.03$, is marked on the heatmaps of the grid search results in Fig. 3c. We also show the 400-ROI FC and SC matrices for the

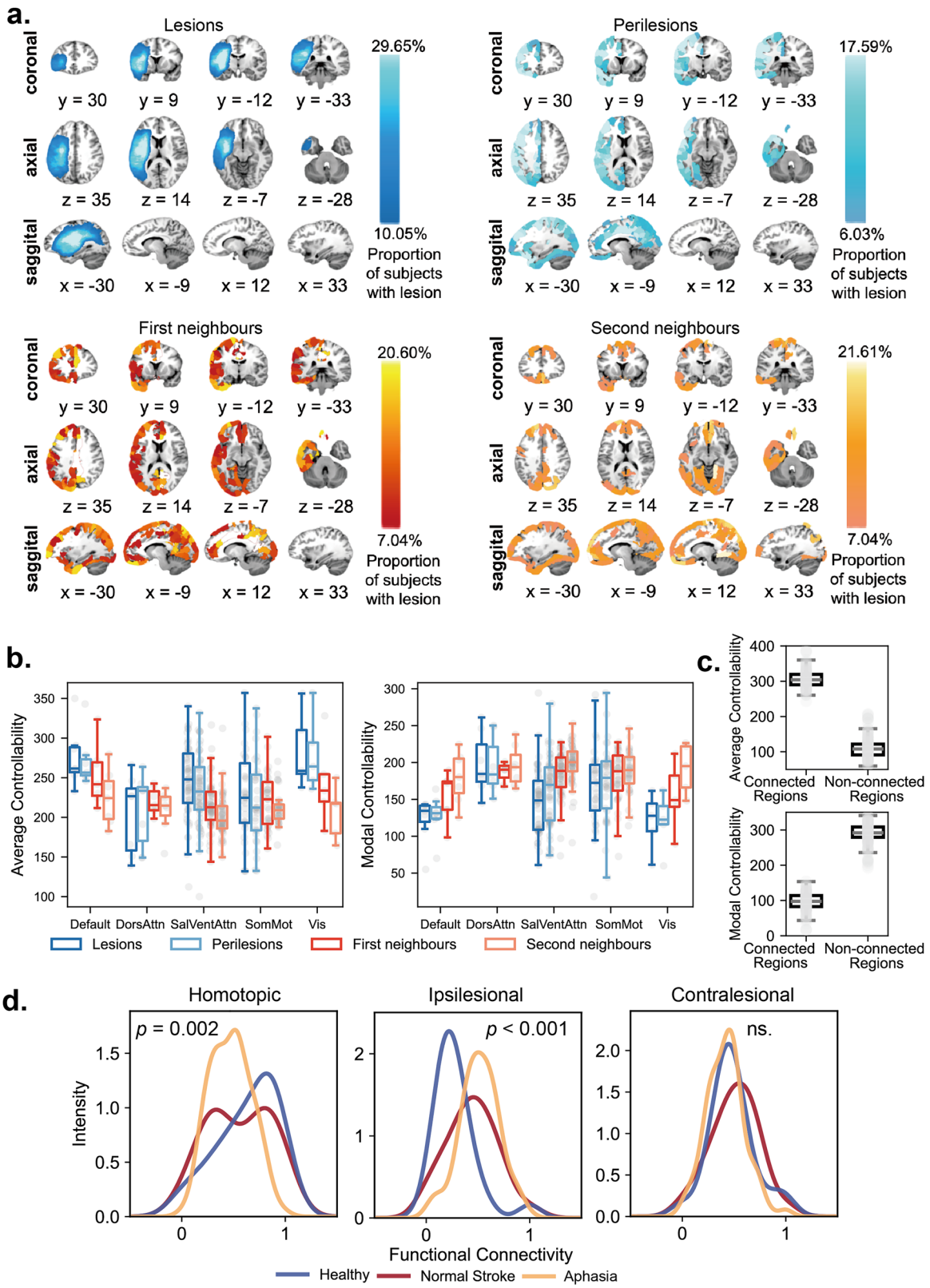

Fig. 2 | Controllability for different spatial locations related to lesions. a Overlay of lesions, perilesions, first and second anatomical neighbours of all patients. **b** Comparison of controllability rank between lesions, perilesions, first and second anatomical neighbors, grouped according to different resting-state networks. A smaller rank value indicates a higher rank for controllability. The central line denotes the median. Dots indicate individual subjects. Boxes show the interquartile (IR) range (25th–75th percentiles), and whiskers extend to values within 1.5 × IR above the 75th and below the 25th percentiles. **c** Comparison of controllability rank for lesion-connected versus not-connected regions. **d** FC statistics of homotopic (interhemispheric homologous), ipsilesional (intra-lesion hemisphere), and contralesional (intra-non-lesion hemisphere).

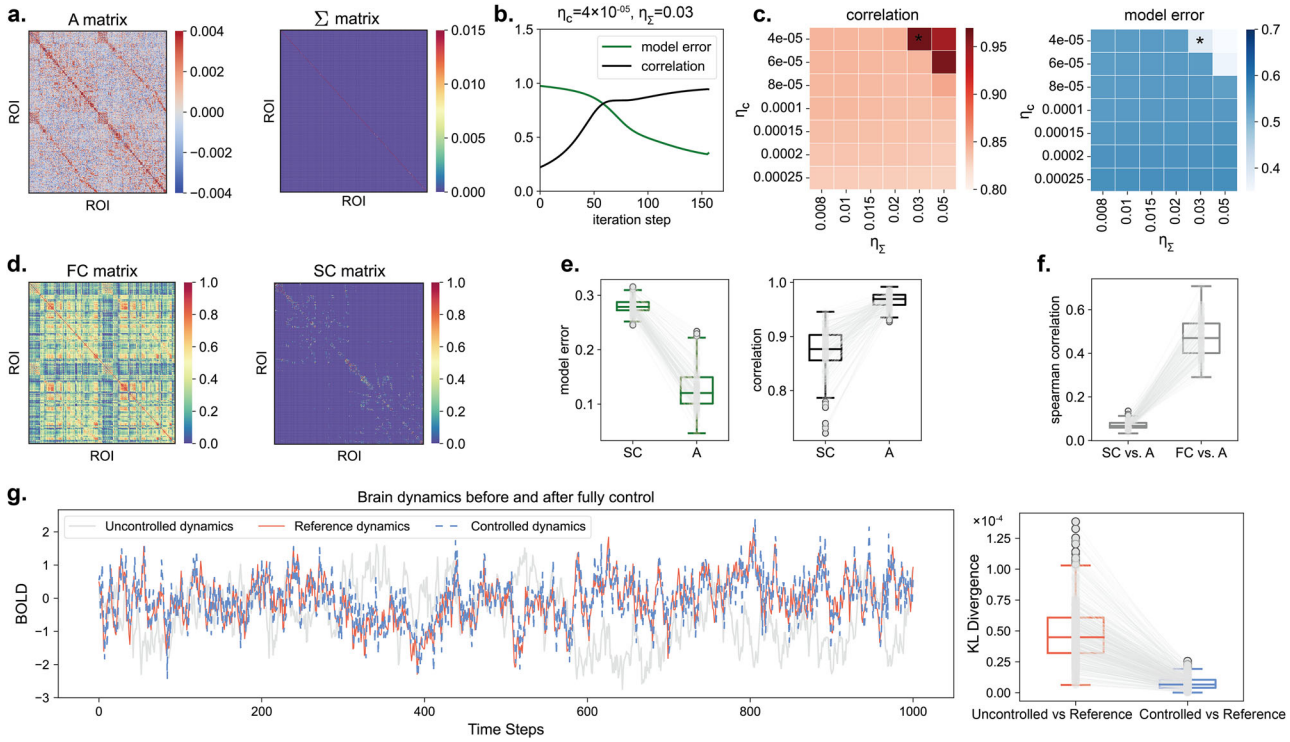

Fig. 3 | The optimized 400-ROI brain network system and the dynamics after fully control (all nodes are controlled using optimal stochastic tracking control) for a representative participant (ID: M2121). a Based on the 400-ROI parcellation, the optimized matrix **A** (ratio of negative/positive connectivities = 1.14 ± 0.04) and **Σ** matrix. **b** The optimization process under the optimal parameter setting. **c** The correlation between the sample data of approximate brain dynamics and the corresponding original fMRI time series data under different parameter settings, along with the error with respect to the target dynamics (where ⋆ indicates the selected optimal parameter setting). **d** The corresponding 400-ROI FC and SC matrix. **e** Statistics of model error and the correlation between the sample data of approximate brain dynamics and the corresponding original fMRI time series data for all participants using matrix **A** and SC. The central line denotes the median. Dots indicate individual subjects. Boxes show the interquartile (IR) range (25th–75th percentiles), and whiskers extend to values within 1.5 × IR above the 75th and below the 25th percentiles. **f** Comparison of correlation between **A** vs. SC, and **A** vs. FC. **g** Based on the 400-ROI parcellation, the target dynamics, the controlled dynamics, and the uncontrolled dynamics (ROI = 1) are visualized as time series. Additionally, a comparison is made between the KL divergence of the controlled dynamics versus the target dynamics, and the KL divergence of the uncontrolled dynamics versus the target dynamics for all nodes in the brain network system.

participant with ID 2121 in Fig. 3d. According to the statistical results, the optimized matrix **A** has a higher correlation and lower model error compared to the SC matrix (Fig. 3e), making it more suitable for dynamics control. Furthermore, the statistical results in Fig. 3f show that the matrix **A** has a higher correlation with the FC matrix than the SC matrix. The results for the 100-ROI system are similar to those for the 400-ROI system, as shown in Supplementary Fig. S1.

Fully control effect using optimal stochastic tracking control

After obtaining the optimal parameters of the brain network dynamics, we performed fully optimal control by controlling all nodes in the fMRI dynamic model of all stroke and aphasia participants, aiming to drive the pathological dynamics toward healthy dynamics (the averaged brain model/dynamics of all healthy participants in the Older Adults dataset). The control effects are shown in Fig. 3g, which visualizes the dynamics (ROI = 1) and statistical results of Kullback-Leibler (KL) divergence of each node/ROI in the 400-ROI brain network system. The results of 100-ROI can be seen in Supplementary Fig. S1. It can be observed that the controlled dynamics closely align with the target dynamics, as evidenced by a small KL divergence observed between the two. In contrast, the uncontrolled dynamics are significantly different from the target dynamics. We also provide several brain dynamics of representative ROIs (ROI = 20, 40, 70, 100 for the 100-ROI system, and ROI = 100, 200, 300, 400 for the 400-ROI system, please see Supplementary Fig. S2). The above results indicate that the statistical similarity of the uncontrolled dynamics to the target dynamics for almost all nodes is larger than that of the controlled dynamics, demonstrating that the tracking control achieved excellent results.

Spatial distribution of tracking energy and its relationship with network controllability

For all four types of aphasia—Anomic, Broca, Conduction, and Global— as well as for normal stroke patients, we further investigated the distribution of tracking energy across the cortex under full control and then quantified its relationship with the intrinsic controllability of brain networks. The tracking energy refers to the control energy necessary to align the pathological brain dynamics of patients with healthy target dynamics within the framework of optimal stochastic tracking control, as detailed in Definition 2. From Fig. 4.a and d, it can be observed that for the 400-ROI brain network system of all five different groups of participants, there is a significant negative correlation between the ranking of tracking energy and the average controllability of the brain network system (Anomic: $R = -0.38$, $p = 5.76 \times 10^{-15}$, Broca: $R = -0.38$, $p = 5.31 \times 10^{-15}$, Conduction: $R = -0.31$, $p = 3.12 \times 10^{-10}$, Global: $R = -0.29$, $p = 3.15 \times 10^{-9}$, Normal stroke: $R = -0.37$, $p = 3.94 \times 10^{-14}$). However, there is no significant correlation between the ranking of tracking energy and modal controllability (Anomic: $R = -0.06$, $p = 0.272$, Broca: $R = 0.01$, $p = 0.863$, Conduction: $R = 0.03$, $p = 0.555$, Global: $R = 0.00$, $p = 0.977$, Normal stroke: $R = -0.08$, $p = 0.132$). For the 100-ROI brain network system, we found highly consistent results (see Supplementary Fig. S3), where the ranking of tracking energy also showed a significant negative correlation with average controllability (Anomic: $R = -0.47$, $p = 6.31 \times 10^{-7}$, Broca: $R = -0.50$, $p = 1.43 \times 10^{-7}$, Conduction: $R = -0.47$, $p = 8.93 \times 10^{-7}$, Global: $R = -0.42$, $p = 1.19 \times 10^{-5}$, Normal stroke: $R = -0.51$, $p = 4.77 \times 10^{-8}$) and no significant correlation with modal controllability (Anomic: $R = 0.07$, $p = 0.518$, Broca: $R = 0.15$, $p = 0.142$, Conduction:

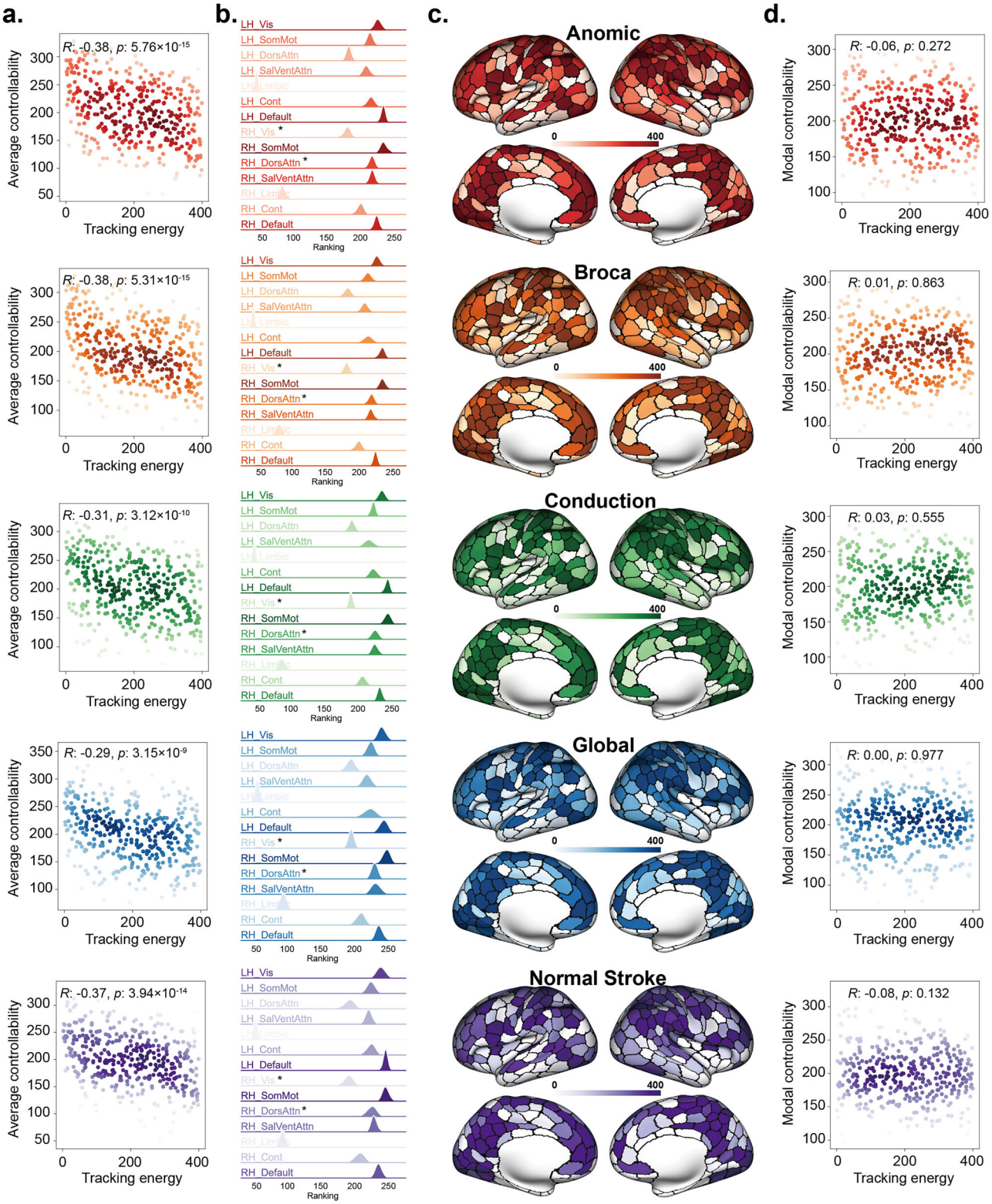

Fig. 4 | The tracking energy ranking (from the largest to the lowest) of the 400-ROI brain network system, from top to bottom: Anomic, Broca, Conduction, Global, Normal Stroke. a The correlation between the ranking of tracking energy and the ranking of average controllability, with *R* values and *p* values provided. **b** The distribution of the averaged ranking of tracking energy among brain network nodes in each resting-state system. ⋆ indicates significant differences between the five groups from top to bottom (using the Kruskal-Wallis test and FDR correction). **c** Visualization of the ranking of tracking energy on the cortex. **d** The correlation between the ranking of tracking energy and the ranking of modal controllability, with *R* values and *p* values provided.

$R = 0.10$, $p = 0.303$, Global: $R = 0.14$, $p = 0.152$, Normal stroke: $R = 0.07$, $p = 0.987$). We further performed dynamics tracking for individual dynamics of healthy participants and obtained a group aggregate of the control performance. We present the main results (the distribution of tracking energy and its correlation with controllability) in Supplementary Fig. S4, from which we observe that the tracking energy and controllability metrics are highly consistent between controlling patients to the averaged dynamic model of healthy participants and averaging the results of controlling patients to each healthy individual's dynamic model.

Additionally, we observed spatially heterogeneous distribution in the ranking of tracking energy across different resting-state systems (Fig. 4b, c). It can be seen that the left and right Limbic regions have the highest rankings, indicating that they consume the highest tracking energy for optimal control. In contrast, the left Vis, Default, and right SomMot regions have the lowest rankings, indicating that they consume the lowest tracking energy. Further, we found that when comparing the five different groups, there were significant differences ($p < 0.05$) in the ranking of tracking energy for the right Vis and right DorsAttn regions (using the Kruskal-Wallis test and FDR correction), as detailed in the Supplementary Fig. S5. For the 100-ROI brain network system, significant differences ($p < 0.05$) were observed only in the right Vis region (Supplementary Figs. S3 and S5). Additionally, we examined the relationship between tracking energy and the topological metrics of network nodes (Supplementary Figs. S6 and S7), and found that for the 400-ROI brain network system, tracking energy is positively correlated with degree and negatively correlated with clustering coefficient.

Characteristics of average controllability and modal controllability

Similarly, we quantified the correlation relationship between the two types of intrinsic controllability and explored their spatial distributions for each group. From Fig. 5a and b, the spatial heterogeneity in the ranking of average controllability across different resting-state systems is not as apparent as the distinct distribution of tracking energy. However, consistent with the significant negative correlation observed between tracking energy and average controllability, the left and right Limbic regions have the lowest rankings for average controllability, and with no significant distributional differences among the five groups. From Fig. 5c, d, it can be seen that for the 400-ROI brain network system, the spatial distribution of modal controllability is more uniform across the cortex, with no significant distributional differences among the five groups. Consistent with previous studies[43–45], there is a significant negative correlation between average controllability and modal controllability for all five groups (as shown in Fig. 5e, Anomic: $R = -0.33$, $p = 1.48 \times 10^{-11}$, Broca: $R = -0.37$, $p = 1.42 \times 10^{-14}$, Conduction: $R = -0.23$, $p = 3.03 \times 10^{-6}$, Global: $R = -0.21$, $p = 1.69 \times 10^{-5}$, Normal stroke: $R = -0.23$, $p = 2.96 \times 10^{-6}$). For the 100-ROI brain network system, the results are completely consistent with those of the 400-ROI system, with a significant negative correlation between average controllability and modal controllability (as shown in the Supplementary Fig. S8, Anomic: $R = -0.45$, $p = 3.10 \times 10^{-6}$, Broca: $R = -0.55$, $p = 4.36 \times 10^{-9}$, Conduction: $R = -0.40$, $p = 8.76 \times 10^{-5}$, Global: $R = -0.38$, $p = 1.09 \times 10^{-4}$, Normal stroke: $R = -0.29$, $p = 3.09 \times 10^{-3}$).

Following previous studies[43,44], we examined the relationship between average/modal controllability and the topological metrics of nodes (Supplementary Figs. S9–S12). Consistent with previous studies[43,44], we found that for the 100-ROI brain network system, average controllability is positively correlated with degree in Anomic, Broca, and Conduction groups. However, for the 400-ROI brain network system, average controllability is negatively correlated with degree and positively correlated with clustering coefficient. This discrepancy may be related to the presence of numerous negative values in the 400-ROI system, as unlike structural and functional brain networks, the optimized brain network system allows the occurrence of negative connectivities. For modal controllability, consistent with previous studies[43,44], significantly negative correlation can be observed between modal controllability and degree, and significantly positive correlation can be observed between modal controllability and clustering coefficient, in which the significance is more pronounced in the 400-ROI system.

Relationship between number of controlled nodes and tracking control effect

To facilitate clinical translation, we attempted to select controlled nodes based on tracking energy to investigate how the brain network system can achieve a basically controllable state at the lowest possible cost. We employed two different strategies for both the 100-ROI and 400-ROI brain network systems: selecting nodes with the largest tracking energy and selecting nodes with the lowest tracking energy. We gradually increased the number of nodes to observe changes in the total KL divergence between the controlled dynamics and the target dynamics, as well as the number of improved nodes (nodes with reduced KL divergence after control compared to before control). We constructed an averaged model for each group, and considering the significant influence of noise on the stochastic tracking control process, we performed 200 simulations for each averaged model to obtain final results.

Figure 6a, b show the changes in KL divergence and the number of improved nodes for the 400-ROI brain network system under the largest and lowest tracking energy strategies, respectively. The shaded gray areas represent the confidence intervals from 200 simulations. It can be observed that when the number of controlled nodes is relatively low, selecting nodes with the lowest tracking energy achieves better control effects than selecting nodes with the largest tracking energy. Further, the high dimensionality of the 400-ROI system modeling makes the system more difficult to control. Under the strategy of selecting the largest tracking energy nodes (Fig. 6a), using 20 nodes can only control around 50% of the system's nodes (200 nodes). Under the strategy of selecting the lowest tracking energy nodes (Fig. 6b), using 20 nodes can only control 60–75% of the system's nodes (250-300 nodes).

The results of 100-ROI can be seen in Supplementary Fig. S13. We can see that for the five different groups, when the number of controlled nodes is 5, selecting the lowest tracking energy nodes can control more than 90% of the system's nodes (Fig. S13b), whereas selecting the largest tracking energy nodes can only control 70–90% of the system's nodes (Fig. S13a). Additionally, within the range of 5–35 nodes, a higher number of nodes does not necessarily result in better control effects.

We further compared the control effects of the five groups in the 100-ROI brain network system with 5 controlled nodes and the 400-ROI brain network system with 20 controlled nodes. The results show that when the system is modeled in 400 dimensions, number of effective controllable nodes is usually below 300 (Fig. 6c). When the system is modeled in 100 dimensions, the normal stroke group is easier to control, with more than 90% of nodes experiencing a decrease in KL divergence (Fig. S13c). Additionally, the tracking energy differs between the 100-ROI and 400-ROI systems. For the 100-ROI system, Anomic and Conduction aphasia require the highest energy, whereas for the 400-ROI system, Global aphasia requires the highest energy. This discrepancy arises partly from the modeling dimensions and partly from the potential asymmetry of controlled nodes.

Comparison with related work

We mainly compare the results of optimal tracking control with the optimal transfer control used in recent studies[18,18,44,46], including the modeling of brain dynamics and control energy, etc.

Simulated brain dynamics with and without neuronal noise. In this section, we first demonstrate the brain dynamics considering neuronal noise compared to the network model without considering noise, as illustrated in Fig. 7. We use the data of a representative participant with ID 2121 as an example, where Fig. 7 corresponds to the results for 400-ROI systems. The results of 100-ROI can be seen in Supplementary Fig. S14. It is evident that the simulated dynamics with neuronal noise more closely approximate the actual dynamics measured by fMRI. In contrast, the dynamics without considering noise tend to converge to

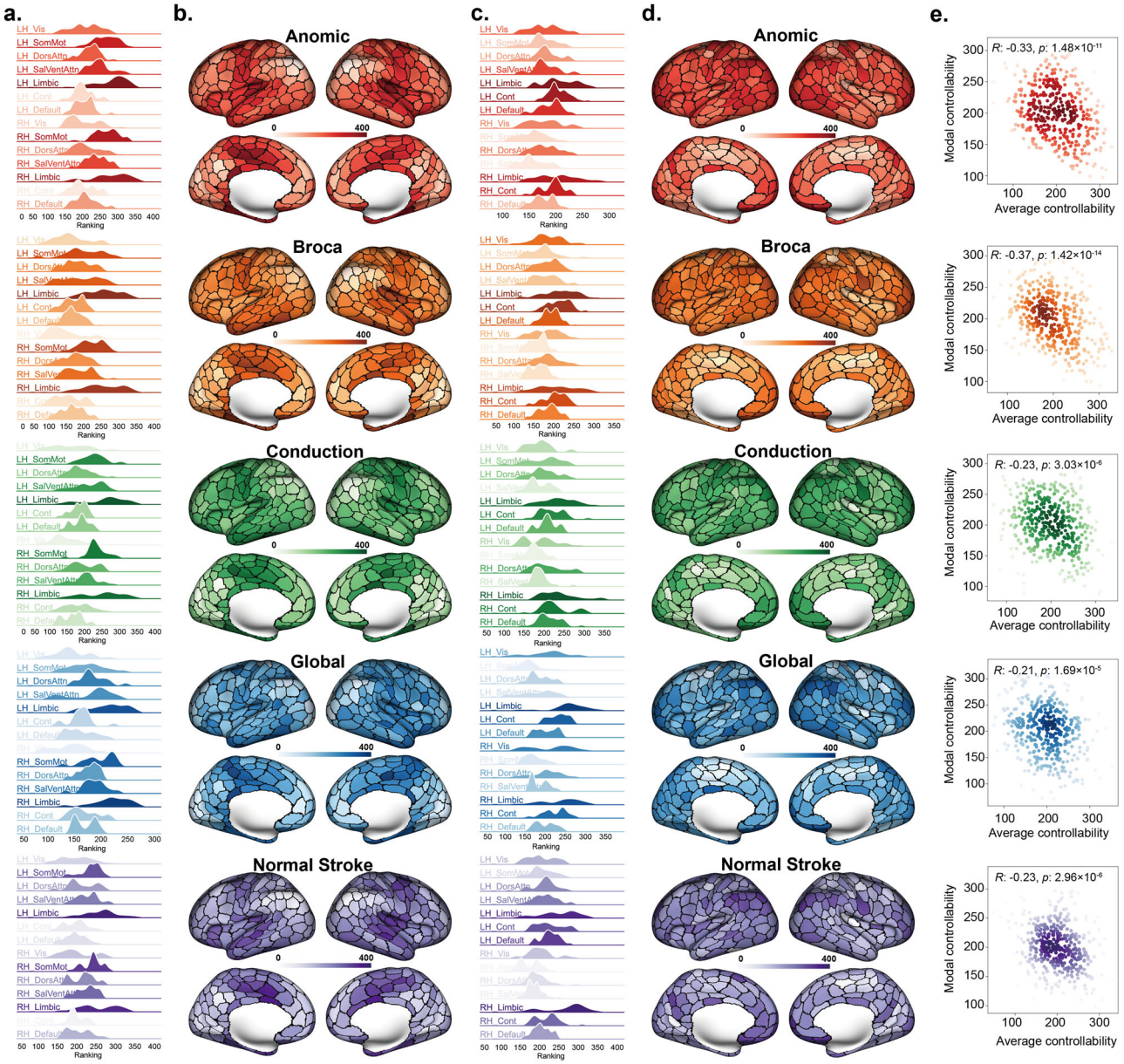

Fig. 5 | The average controllability and modal controllability ranking (from the largest to the lowest) of the 400-ROI brain network system, from top to bottom: Anomic, Broca, Conduction, Global, Normal Stroke. a The distribution of the averaged ranking of average controllability among brain network nodes in each resting-state system. **b** Visualization of the ranking of average controllability on the cortex. **c** The distribution of the averaged ranking of modal controllability among brain network nodes in each resting-state system. **d** Visualization of the ranking of modal controllability on the cortex. **e** The correlation between the ranking of average controllability and the ranking of modal controllability, with *R* values and *p* values provided.

zero over time, due to the eigenvalues of the coupling matrix **A** being all less than zero, leading to the convergence of the state **x**.

Control energy of optimal state transfer control. Although the results of optimal state transfer control and optimal stochastic tracking control cannot be directly compared, we can quantify their relationships with the intrinsic characteristics of the brain system to explore any correlated features. For optimal state transfer control, we used clustering methods to select four representative discrete brain states as target states for both the 100-ROI and 400-ROI brain systems. We then used the peak states of each individual participant as the original states and pushed them to the four target states. For the 400-ROI system, Fig. 8a provides visualizations of the spatial distributions of the four target states, while Fig. 8b quantifies the average distribution of these states within each resting-state system. The results for the 100-ROI system can be seen in Supplementary Fig. S15. It can be observed that the four states exhibit distinct spatial distribution characteristics, and the four states in the 100-ROI and 400-ROI brain systems can be matched to each other. Specifically, state 1 of the 100-ROI system corresponds to state 4 of the 400-ROI system, state 2 of the 100-ROI system corresponds to state 1 of the 400-ROI system, state 3 of the 100-ROI system corresponds to state 2 of the 400-ROI system, and state 4 of the 100-ROI system corresponds to state 3 of the 400-ROI system. We retained the original order of the clustering results for visualization, which does not substantially affect the results.

For the 400-ROI system, Fig. 8c illustrates the relationship between the energy of optimal state transfer control and other features (i.e., tracking energy, average controllability, modal controllability, and the value of the state itself) across five different groups. For the 400-ROI brain network system (Fig. 8c), despite identifying more statistically significant correlations between the control energy and three features beyond and state value, most

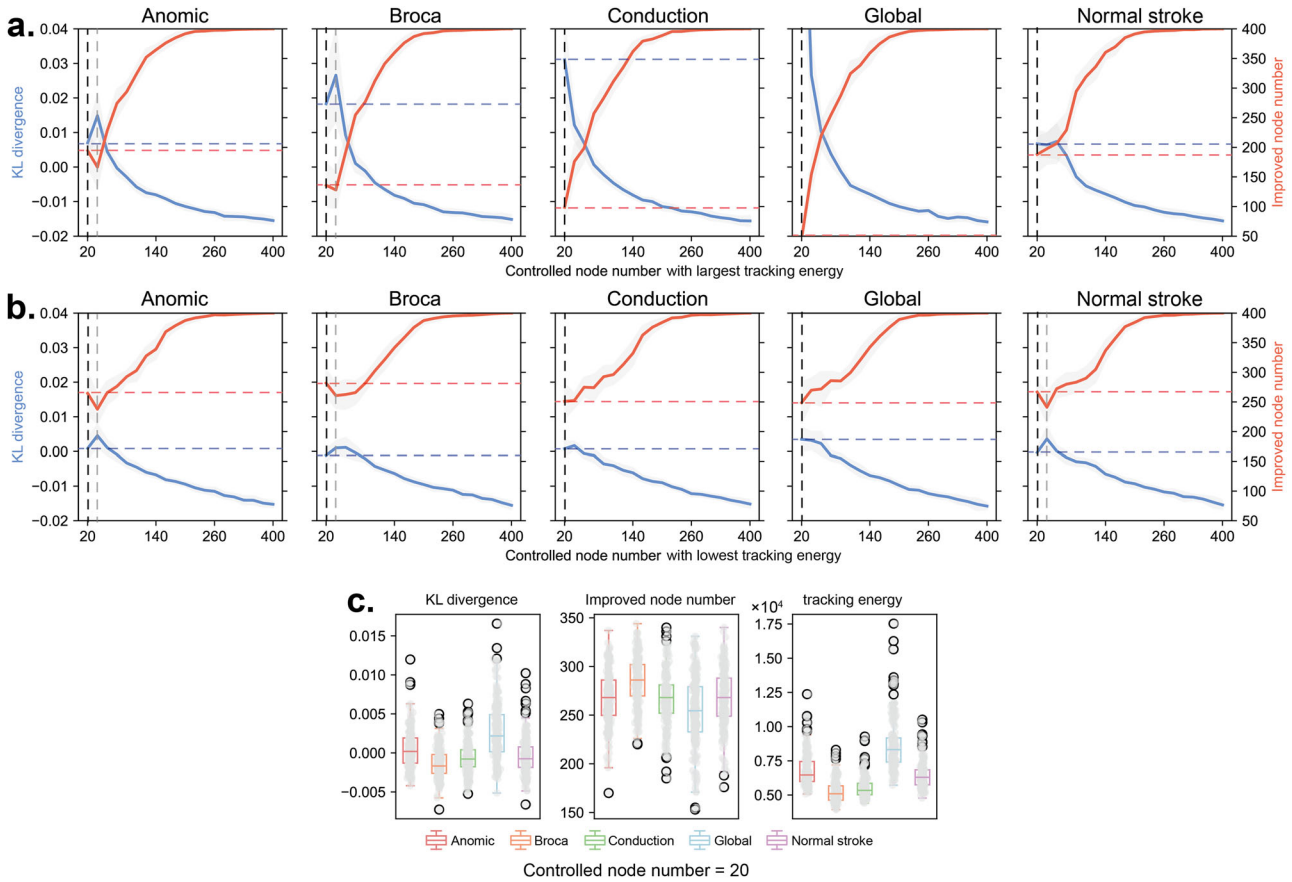

Fig. 6 | The control effects with different numbers of control nodes, from left to right: Anomic, Broca, Conduction, Global, Normal Stroke. The black dashed line represents the minimum number of controllable nodes (20 for 400-ROI system), while the gray dashed line represents the number of controllable nodes at the inflection point of KL divergence and the improved node number. **a** For the 400-ROI brain network system, the total KL divergence of the system and the number of nodes with improved KL divergence when control nodes are incrementally added in descending order of tracking energy. Controlled nodes are added in increments of 20. **b** For the 400-ROI brain network system, the total KL divergence of the system and the number of nodes with improved KL divergence when control nodes are incrementally added in ascending order of tracking energy. Controlled nodes are added in increments of 20. **c** The control effect for the 400-ROI brain network system when the controlled nodes are the 20 nodes with the lowest tracking energy. The central line denotes the median. Boxes show the interquartile (IR) range (25th-75th percentiles), and whiskers extend to values within 1.5 × IR above the 75th and below the 25th percentiles.

significant correlations are concentrated between the energy of optimal state transfer control and the target state itself. Similarly, Fig. S15c shows similar results for the 100-ROI system. These results indicate that the energy of optimal state transfer control is highly dependent on the chosen target state itself, rather than the intrinsic characteristics of the brain network system.

Discussion

To provide insights into the effects of brain stimulation and optimal paradigms, this investigation introduces optimal stochastic tracking control for brain network dynamics. This approach addresses factors that were not considered in previous studies. Building upon this foundation, the investigation delves into the spatial distribution of stochastic tracking control energy and its correlation with the inherent characteristics of the brain network system. Furthermore, we draw indirect comparisons with the outcomes of optimal state transfer control strategies. Finally, we attempt to determine the minimal cost at which the brain network system can achieve an acceptable control effect. The following discussion will summarize our research findings.

Average controllability typically measures the ability of driving a system to a nearby state, while modal controllability measures the ability of driving a system to a hard-to-reach state[43,44]. Consistent with the findings of limited studies on stroke-related controllability[45], we observed a consistent negative correlation between average controllability and modal controllability. However, existing research has focused on the controllability of the lesion regions. We further discovered that regions closer to the lesion exhibit higher modal controllability and lower average controllability. This result is more pronounced in the comparison between lesion-connected and non-connected regions. This finding suggests that lesions may influence the global network controllability by destroying structural connections. Damage to the structural connections in the lesional/connected regions makes it difficult to maintain stable and typical states similar to healthy brain states (leading to lower average controllability). However, the atypical reorganization of the network structure may make them more likely to drive the brain network into different modes in dynamic control (higher modal controllability).

The field of brain network control has experienced substantial advancements since the representative paper by Gu et al.[43], progressing from studies on network controllability[43,45] to optimal control of linear dynamics[18,44,46,47]. Gu et al. proposed that cognitive control can be effectively explained by the network controllability properties of specific brain regions, which facilitate the transition of the brain network from one state to a target cognitive state[43]. This sparked significant interest in the possibility of customizing input signals to guide the brain along a 'controlled' trajectory and into the desired target state. Given the growing interest in brain stimulation techniques (including TMS[10], direct current stimulation[48], chemogenetic applications[49], and optogenetic stimulation[50]), this question is highly relevant with numerous clinical applications. Brain states are typically defined by discrete states at a single

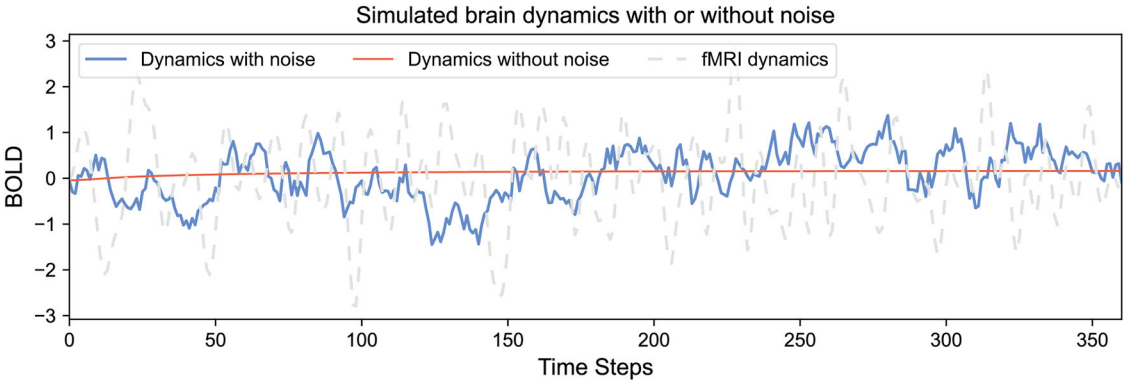

Fig. 7 | The simulated brain dynamics with noise ($\dot{\mathbf{x}}(t) = \mathbf{A}\mathbf{x}(t) + \mathbf{w}(t)$) and without noise ($\dot{\mathbf{x}}(t) = \mathbf{A}\mathbf{x}(t)$) for a representative participant (ID: M2121). Based on the 400-ROI parcellation, the fMRI dynamics, the simulated dynamics with noise, and the simulated dynamics without noise (ROI = 1) are visualized as time series.

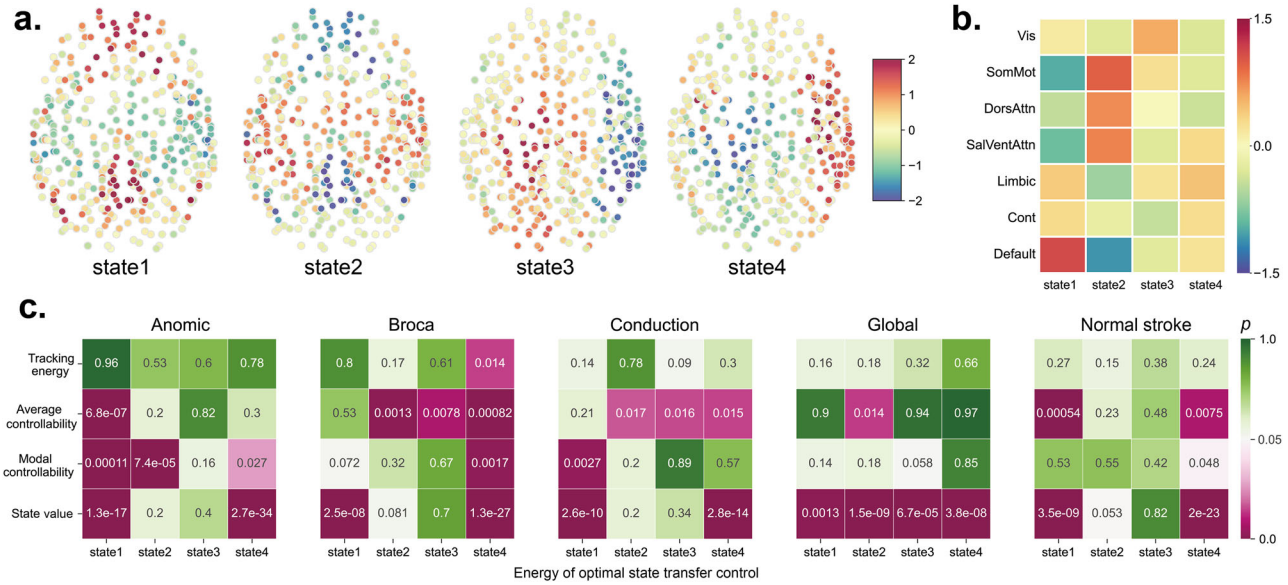

Fig. 8 | Results of optimal state transfer control energy. a The four target states of the 400-ROI brain network system were obtained through clustering. **b** The distribution of the four target states of the 400-ROI brain network system in each resting-state system. **c** For the 400-ROI brain network system, the p-values of the correlations between the optimal state transfer control energy for the four target states and tracking energy, average controllability, modal controllability, and the states themselves. Significance thresholds are defined by 0.05, with values above 0.05 shown in green and values below 0.05 shown in red.

time point, usually obtained through functional brain activity measurements such as fMRI[46,47] and ECoG[18]. And representative brain states are then selected and identified through clustering methods. This strategy presents challenges due to the brain's ability to generate multiple brain states even within a short period. The primary advantage of optimal tracking control lies in its ability to operate on dynamic processes/trajectories. This approach is not affected by state selection and enables the tracking of dynamic characteristics that state transfer control cannot achieve. It potentially represents a significant direction for future brain network optimal control research.

In contemporary research on optimal brain network control, the consideration of neuronal noise is frequently disregarded. When referring to neuronal noise, they refer to the intrinsic random fluctuations within neural networks[51]. Under the linear dynamics assumption in current studies[18,44,46,47], the brain network is a linear time-invariant system. When noise and external disturbances are not considered, the dynamics are described by $\dot{\mathbf{x}}(t) = \mathbf{A}\mathbf{x}(t)$, where the brain state changes over time solely in relation to the coupled matrix $\mathbf{A}$. For this linear system, the eigenvalues of $\mathbf{A}$ are required to have negative real parts to ensure the stability of the brain network dynamics. When considering $\mathbf{w}(t)$, the stochastic characteristics of neuronal activity at the microscopic level are incorporated. A recent study by Kamiya et al.[52] employed a similar modeling approach incorporating noise in conjunction with optimal state transfer control. Although it cannot fully replicate the actual dynamics of brain networks, the consideration of neuronal noise represents a significant advancement in the field of brain network control.

Our results provide a clear correlation between tracking energy and the intrinsic characteristics of the brain network system, potentially benefiting from the complexity of the control target we considered. Despite the influence of neuronal noise, the target is a time series characterized by fixed statistical properties. After considering both the system and the noise variance, the tracking results are highly robust. The significant negative correlation between tracking energy and average controllability indicates that nodes that can easily drive the network to nearby states require correspondingly lower tracking energy. In contrast, for the optimal state transfer control strategy, the control energy is highly correlated with the selected state values, and its relationship with the intrinsic characteristics of the brain network system is unclear. A single brain state can be represented as a discrete vector, which presents some challenges in accurately modeling various pathological or healthy states. Therefore, the tracking energy obtained from dynamics tracking may offer higher stability and universality for brain stimulation therapy, as it achieves effective dynamics tracking

while considering noise, and the results are correlated with brain network characteristics.

Over the past decade, whole-brain network models have become pivotal in advancing our understanding of the mechanisms underlying differences in brain states[53–55]. These models provide a computational framework that integrates neuroimaging data to simulate the dynamic interactions among brain regions, offering a powerful tool for investigating large-scale neural activity and its perturbations. Building on this foundational approach, dynamic sensitivity analysis (DSA) has emerged as an integrative framework that leverages whole-brain models to identify optimal stimulation strategies for restoring spatiotemporal brain dynamics across diverse cognitive and clinical states[56–58]. Unlike classical control theory-based methods, which primarily focus on driving the system to follow a predefined target trajectory or state through external feedback controllers, DSA is concerned with restoring the equilibrium of spatiotemporal brain dynamics[57]. This is achieved by iteratively adjusting model parameters during the fitting process to minimize discrepancies between simulated and empirical dynamics. The objective functions in DSA are typically designed to minimize the probability of metastable substates (PMS) or other statistical metrics that characterize key features of brain dynamics[57]. It is noteworthy that the objective of DSA lies between optimal transfer control and optimal tracking control. While transfer control aims to achieve a representative brain state at a single time point and tracking control endeavors to regulate the entire temporal evolution of brain dynamics, DSA focuses on capturing and optimizing the statistical properties underlying these dynamics. Furthermore, due to its grounding in whole-brain modeling, DSA can be easily integrated with nonlinear dynamics. The potential integration of DSA with classical control theory remains a promising direction for future research, offering significant opportunities to enhance our understanding of brain dynamics and to develop therapeutic strategies.

Existing studies have proposed various brain parcellation templates at different scales[39,59–61]; however, there is currently no standard criterion for brain parcellation. For modeling purposes, it is straightforward that increasing the model dimensions can provide a more accurate framework. However, this also entails greater computational challenges and requires additional experimental resources to improve the accuracy of higher-dimensional models. For control purposes, our results reveal that different scales of brain network modeling may result in varying control effects even with the same proportion of controlled nodes. For instance, if the cortex is modeled with 100 dimensions, selecting the five nodes with the lowest tracking energy for control can achieve an acceptable control effect for dynamics tracking (with the dynamics of over 90% of the nodes being improved). However, if the system is modeled with 400 dimensions, the control cost (i.e., the number of control nodes required) would significantly increase. Actually, a higher-dimensional model implies more detailed divisions of brain regions, while non-invasive brain stimulation typically affects a specific spatial range. Therefore, higher-dimensional models may necessitate adjustments to the control algorithm. In practical brain stimulation techniques such as TMS[10], stimulation localization can be accurate, but this does not mean that the affected brain region is small. There are various types of TMS stimulation coils. The circular coil has a lower focus compared to the figure-8 coil, while the H-coil has poorer focus but deeper stimulation. The double-cone coil performs better than the H-coil in both depth and focus[62]. When we discuss the possibility of applying NCT in clinical settings, the size of the brain models is related to the focus of TMS coil. If the TMS coil has a lower focus, it means we need to use a brain parcellation with a smaller scale. Further, current research is beginning to model stimulation in a diffusive manner to simulate the impact of brain stimulation on other uncontrolled brain regions[46,63]. Undoubtedly, the extent of the brain region affected by a single stimulation and its diffusion effect will influence the estimation of control cost.

Additionally, it is worth noting that, with a smaller number of control nodes, the dynamics of the stroke group seem easier to control compared to the aphasia group (Supplementary Fig. S13, for the 100-ROI system). However, for the 400-ROI system, the Broca group seems easier to control (Fig. 6). In fact, this conclusion is not generalizable. Firstly, results exhibit variability depending on the number of control nodes. Secondly, the control node selection strategy implemented is fixed, and selecting control nodes based solely on tracking energy may not necessarily be the most optimal approach. Consequently, further research is necessary to either corroborate or rectify the aforementioned findings.

One of the significant challenges in applying network control theory to practical neural modulation experiments is an ambitious goal: controlling the entire brain's activity. While a sufficiently connected network can theoretically be controlled by a single driving node, in practice, a substantial portion of the total nodes must be utilized as driving nodes to achieve this at a feasible energy cost[64,65]. For large networks, this necessitates the use of numerous driving nodes. To date, most TMS applications are based on single-channel TMS, combined with neuro-navigation systems for precise and repeatable targeting of external brain regions[66]. Single-channel TMS technology has been extended to dual-focus configurations by employing two independent coils and stimulators[67]. Another study demonstrated a system capable of accommodating up to four channels, thereby enabling more flexible spatiotemporal stimulation control[68]. Although the concept of TMS arrays is straightforward, in practical clinical settings, single and double-coil devices remain the predominant choice. This limitation, as it can only stimulate one (or two) sites simultaneously[69], presents a challenge in achieving multi-node control of brain networks.

Limitation and future directions

The optimal stochastic tracking control framework implemented in this study represents a well-established method in control theory that jointly optimizes tracking performance and energy efficiency. Our empirical results demonstrate that multi-node intervention is required to achieve satisfactory dynamic synchronization. Future investigations could explore pinning control methodologies[70,71], though the inherent trade-off between reduced node numbers and increased energy requirements presents a non-trivial optimization challenge.

While our current modeling approach encompasses the complete cortical network, subsequent research should prioritize targeted examinations of neurological mechanisms, particularly in post-stroke aphasia. Focused studies on language-related cortical regions, such as the inferior frontal gyrus (IFG)[72,73], may yield more clinically actionable insights for stimulation protocols.

Theoretical extensions incorporating nonlinear dynamical systems (e.g., Wilson-Cowan or neural mass models) could provide superior characterization of complex neural phenomena and state-dependent control properties. However, such advancements would necessitate solutions to the associated computational and parameter estimation challenges. Parallel investigations of alternative noise models (e.g., colored noise, non-Gaussian distributions) may further improve model fidelity and adaptive capabilities.

Finally, the methodological framework developed here shows promising generalizability to various neurological conditions[18,20–22] requiring neuromodulation interventions. Expansion to incorporate multimodal neuroimaging datasets (fMRI/electrophysiology) could further enhance the clinical applicability across diverse patient populations.

Methods

Participants and data acquisition

Dataset 1. Diffusion-weighted imaging (DWI) and resting-state fMRI data were obtained from the University of South Carolina and the Medical University of South Carolina[74]. The Institutional Review Board (IRB) at the University of South Carolina determined that the study was exempt from further ethical review. All ethical regulations relevant to human research participants were followed. The final dataset comprised 148 post-stroke aphasia (including four aphasia types: Anomic, Broca, Conduction, Global) patients and 26 normal stroke patients, after excluding those with head motion greater than 3mm. Participants were instructed to remain still, keep their eyes open, and stay awake during the scan. All fMRI images were collected

using a Siemens Trio 3.0T scanner with a 16-channel head coil. For each participant, the fMRI scan closest to the time of stroke onset was selected for further analysis.

Dataset 2. For finding target states/dynamics for patients, a target group of 28 healthy old participants underwent whole-brain imaging at the Gateway MRI Center at UNCG, utilizing a Siemens 3.0T Tim Trio MRI scanner with a 16-channel head coil, was selected for analysis. The study received approval from the IRB at the University of North Carolina at Greensboro[75]. All ethical regulations relevant to human research participants were followed. Resting-state fMRI data were acquired following anatomical scans, with 300 measurements collected during the 10 min scanning sessions. Participants were instructed to remain still, awake, and with their eyes open throughout the procedure. Functional imaging was performed using echo-planar imaging sequences sensitive to blood oxygen level-dependent (BOLD) contrast, with a slice thickness of 4.0 mm, 32 slices, a TE of 30 ms, a TR of 2000 ms, and a flip angle of 70°. The scans covered the entire cerebral cortex and portions of the cerebellum. The primary objective of this dataset was to explore how connectome-based modeling of intrinsic functional connectivity (FC) within the default mode network could predict memory discrimination differences between young and older adults. Statistical information of participants for population number, age, and Western Aphasia Battery (WAB) score is presented in Table 1.

Table 1 | Participants' information of datasets

Group	Number of population	Age ± (std)	WAB Score ± (std)
Anomic	46	62 ± 11.1	87 ± 6.2
Broca	65	62 ± 10.7	44 ± 17.4
Conduction	23	61 ± 11.7	63 ± 15.2
Global	14	62 ± 9.0	17 ± 7.7
Normal stroke	26	62 ± 11.9	98 ± 1.9
Healthy	36	69.82 ± 5.6	Not applicable

Data preprocessing

For the fMRI raw scan data in the above two datasets, we performed preprocessing operations. The first ten volumes of each scan were excluded to ensure magnetic stability and to optimize the generation of a consistent BOLD activity signal. The preprocessing pipeline was implemented utilizing the CONN toolbox[76]. Subsequently, the fMRI data underwent the following procedures:

1. Correction for slice timing;
2. Realignment to correct for head motion;
3. Normalization to a 3 mm MNI space using an EPI template provided by the CONN software package;
4. Application of linear temporal detrending to remove the linear drift of the BOLD signal;
5. Covariate regression, including the white matter signal, cerebrospinal fluid (CSF) signal, and head motion signal, utilising the Friston-24 Parameters strategy;
6. Temporal filtering with a bandwidth of 0.01-0.1 Hz.

We utilized the 100 and 400-ROI parcellation templates from Schaefer2018 parcellation[39] at different scales to parcel the cortex, and for further estimation of brain network systems. The Schaefer2018 atlas parcels the cortex into 100 to 1000 ROIs, which can be further subdivided into either 7 or 17 subnetworks at coarse or fine levels, respectively. The Schaefer2018 atlas is multi-scale and presents a significant advantage in our investigation, enabling the cortex to be partitioned into systems of different sizes (ranging from 100 to 1000) based on the same principle. This feature proves particularly beneficial for investigating system-scale sizes and the impact of distinct subnetworks on network control. Other atlases, such as the Power Atlas[77], Gordon[78], and BrainNetome[79], employ fixed partition scales. In this paper, we selected the Schaefer100 and Schaefer400 scales, which have been further classified into 7 subnetworks, as the basis for modeling the brain cortical network. The brain cortex is parcellated using the Schaefer atlas, and the average time series of BOLD signals for each region is extracted. The Fisher z-transformed Pearson correlation coefficient is used to measure functional connectivity (FC). We employed a regression-out approach (one of the most used harmonization techniques[80,81]) for preprocessed data to eliminate any potential factors that could influence the results, including sites, equipment, acquisition parameters, and the age and gender of individuals.

We performed DWI preprocessing, fiber tracking, and connectivity matrix construction using FMRIB Software Library (FSL) and MRtrix3. The entire process includes denoising, mask generation, registration and parcellation mapping, fiber direction estimation, and fiber tracking. Fibers for each participant are matched with brain regions from Schaefer2018 parcellation (100 and 400 ROIs), forming structural connectivity (SC) matrices weighted by the number of probabilistic streamlines between brain regions. The weights are then scaled to a range of 0 to 1.

Brain network dynamic models

NCT requires the establishment of a brain dynamic model, along with equations describing the connectivity between brain regions. In this context, we employ the stochastic linear time-invariant model:

$$\dot{\mathbf{x}}(t) = \mathbf{A}\mathbf{x}(t) + \mathbf{w}(t), \tag{1}$$

where $\mathbf{x}(t)$ is an $N \times 1$ vector that represents the brain state (i.e., the BOLD time series for fMRI measurement) at time t, and N is the number of brain regions. In the network adjacency matrix (or coupled matrix) $\mathbf{A}$, each a_{ij}-th element gives the quantitative anisotropy between region i and region j. $w(t)$ is formally characterized as a zero-mean Gaussian white noise process with $E[\mathbf{w}(t)] = \mathbf{0}$ and $\mathrm{Var}[\mathbf{w}(t)] = \mathbf{\Sigma}^2$.

The coupled matrix $\mathbf{A}$ in Eq. (1) determines the brain network dynamics, which was described by a multivariate Ornstein-Uhlenbeck process[82–84]:

$$\dot{x}_i(t) = -\frac{x_i(t)}{\tau_{\mathbf{x}}} + \sum_{j \neq i} \mathbf{C}_{ji} x_j(t) + w_i(t). \tag{2}$$

where the time constant $\tau_{\mathbf{x}}$ abstracts the intrinsic dynamics of each ROI, each activity $x_i(t)$ of node i decays exponentially according to the time constant $\tau_{\mathbf{x}}$ and evolves depending on the activity of other populations. The network effective connectivity (EC) between different ROIs, embodied by the matrix $\mathbf{C}$, whose topological skeleton is determined by structural data. The fluctuating inputs $w_i(t)$ are independent and correspond to a diagonal variance matrix $\mathbf{\Sigma}$. In matrix notation, it is:

$$\dot{\mathbf{x}}(t) = \mathbf{J}\mathbf{x}(t) + \mathbf{w}(t). \tag{3}$$

All $x_i(t)$ have zero mean, of which the spatiotemporal covariances are denoted by Q_τ^{ij}, where $\tau \in \{0, 1\}$ is the time lag, and they satisfy the following consistency equations:

$$\mathbf{J}^\top \mathbf{Q}_0 + \mathbf{Q}_0 \mathbf{J} = -\mathbf{\Sigma}, \tag{4}$$

$$\mathbf{Q}_1 = \mathbf{Q}_0 e^{\mathbf{J}}, \tag{5}$$

where e denotes the matrix exponential, superscript $\top$ denotes the matrix transpose. $\mathbf{J}$ is the Jacobian of the dynamical system, can be considered as a appropriate estimation for $\mathbf{A}$, which depends on the time constant τ_x and the

network EC:

$$J_{ji} = -\frac{\delta_{ji}}{\tau_x} + C_{ji}, \tag{6}$$

where δ_{ji} is the Kronecker delta.

Parameter estimation of network dynamic model using gradient descent optimization

Most studies treat the networks extracted from structural imaging as the matrix **A** in network control; however, it may not necessarily correspond to the measured brain network dynamics. For obtaining a fine estimation of **J** in Eq. (6) for brain network dynamics, i.e.,8 the estimation of **A**, we tune the above model in Sec. 8 to make its covariance matrices $\mathbf{Q}_0$ and $\mathbf{Q}_1$ reproduce the empirical $\hat{\mathbf{Q}}_0$ and $\hat{\mathbf{Q}}_1$ according to previous studies[83,84], which can be calculated as follows: For a session of T time points, we denote the BOLD time series by $s_i(t)$ for each region $1 \le i \le N$ with time indexed by $1 \le t \le T$. The mean signal is $\bar{\mathbf{s}}_i = \frac{1}{T}\sum_t s_i(t)$ for all i. Following previous studies[83,84], two BOLD covariance matrices without and with time lag are:

$$\hat{Q}_0^{ij} = \frac{1}{T-2}\sum_{1 \le t \le T-1}(s_i(t) - \bar{s}_i)(s_j(t) - \bar{s}_j), \tag{7}$$

$$\hat{Q}_1^{ij} = \frac{1}{T-2}\sum_{1 \le t \le T-1}(s_i(t) - \bar{s}_i)(s_j(t+1) - \bar{s}_j). \tag{8}$$

Pearson correlation K_{ij} can be calculated from the covariances in Eq. (7) and (8):

$$K_{ij} = \frac{\hat{Q}_0^{ij}}{\sqrt{\hat{Q}_0^{ii}\hat{Q}_0^{jj}}}. \tag{9}$$

The iterative optimization procedure for **C** in Eq. (6) is related to a concept of natural gradient descent that accounts for the non-linearity of the mapping between **J** and the matrix pair $\mathbf{Q}_0$ and $\mathbf{Q}_1$:

$$\tau_{ac} = -\frac{\sum_i \log\left(\hat{Q}_0^{ii}\right) - \sum_i \log\left(\hat{Q}_1^{ii}\right)}{N \cdot \tau_{TR}}, \tag{10}$$

where τ_{TR} is the time resolution (TR) value of fMRI in seconds.

The difference matrices $\Delta\mathbf{Q}_0 = \hat{\mathbf{Q}}_0 - \mathbf{Q}_0$ and $\Delta\mathbf{Q}_1 = \hat{\mathbf{Q}}_1 - \mathbf{Q}_1$ determine the model error:

$$E = \frac{1}{2}\frac{\| \Delta\mathbf{Q}_0\|^2}{\| \hat{\mathbf{Q}}_0\|^2} + \frac{1}{2}\frac{\| \Delta\mathbf{Q}_1\|^2}{\| \hat{\mathbf{Q}}_1\|^2}. \tag{11}$$

The Jacobian update is applied to decrease the model error E at each optimization step:

$$\Delta\mathbf{J} = \mathbf{Q}_0^{-1}[-\Delta\mathbf{Q}_0 + \Delta\mathbf{Q}_1 e^{\mathbf{J}}]. \tag{12}$$

A update that is more robust to empirical noise is:

$$\Delta\mathbf{J} = \mathbf{Q}_0^{-1}\Delta\mathbf{Q}_0 + \Delta\mathbf{Q}_0\mathbf{Q}_0^{-1} + \mathbf{Q}_1^{-1}\Delta\mathbf{Q}_1 + \Delta\mathbf{Q}_1\mathbf{Q}_1^{-1}. \tag{13}$$

Optimal state transfer control requires the coupled matrix **A** to be symmetric. To ensure the symmetry of the coupled matrix, we modified the Jacobian update $\Delta\mathbf{J}$ as follows:

$$\begin{aligned}\Delta\mathbf{J} = {} & \mathbf{Q}_0^{-1}\Delta\mathbf{Q}_0 + \Delta\mathbf{Q}_0\mathbf{Q}_0^{-1} + 1/2\left[\left(\mathbf{Q}_1^{-1}\Delta\mathbf{Q}_1\right)^{\top} + \mathbf{Q}_1^{-1}\Delta\mathbf{Q}_1\right] \\ & + 1/2\left[\left(\Delta\mathbf{Q}_1\mathbf{Q}_1^{-1}\right)^{\top} + \Delta\mathbf{Q}_1\mathbf{Q}_1^{-1}\right].\end{aligned} \tag{14}$$

From the Jacobian update $\Delta\mathbf{J}$, the connectivity update was obtained:

$$\Delta C_{ij} = \eta_{\mathbf{C}}\Delta J_{ij}. \tag{15}$$

Non-negativity is imposed on the EC values during the optimization. To take properly the effect of cross-correlated inputs into account, the $\mathbf{\Sigma}$ update is:

$$\Delta\mathbf{\Sigma} = -\eta_{\mathbf{\Sigma}}\left(\mathbf{J}^{\top}\Delta\mathbf{Q}_0 + \Delta\mathbf{Q}_0\mathbf{J}\right). \tag{16}$$

Finally, the time constant τ_x can also be tuned as:

$$\Delta\tau_x = \eta_{\tau}\left(\tau_{ac} + \frac{1}{\lambda_{\max}}\right), \tag{17}$$

where $\lambda_{\max}$ is the maximum negative real part of the eigenvalues of **J**. Repeating the parameter updates, the best fit of matrix **J** corresponds to the minimum model error E.

Optimal stochastic tracking control

Our long-term goal is to use the model described above to predict optimal stimulation parameters, i.e., network control. In the network dynamics control model, we first consider two important factors: one is the stochastic fluctuation in the brain dynamics, which may represent spontaneous activity or noise in brain networks; the other is the optimal control from one network dynamics to a target dynamics, which can be seen as a tracking problem in the control domain, rather than pushing one discrete brain state to another. Given the linear stochastic system state equation like Eq. (1) with input:

$$\dot{\mathbf{x}}(t) = \mathbf{A}\mathbf{x}(t) + \mathbf{B}\mathbf{u}(t) + \mathbf{w}(t). \tag{18}$$

where the input matrix **B** was defined to allow input dominated by the stimulation region of interest (ROI). The output equation is:

$$\mathbf{z}(t) = \mathbf{D}\mathbf{x}(t), \tag{19}$$

where $\mathbf{z}(t)$ is a N-dimensional output vector. In brain network systems, the matrix **D** can be considered as an identity matrix, implying that $\mathbf{z}(t) = \mathbf{x}(t)$.

Let the N-dimensional target vector $\mathbf{z}_r(t)$ be the output of the target dynamic model under the influence of stochastic noise. The state equation of the target model is known to be:

$$\dot{\mathbf{x}}_r(t) = \mathbf{A}_r\mathbf{x}_r(t) + \mathbf{w}_r(t). \tag{20}$$

where $\mathbf{w}_r(t)$ is stochastic noise with zero mean and variance matrix $\mathbf{Q}_r$. The output equation of the target model is:

$$\mathbf{z}_r(t) = \mathbf{D}\mathbf{x}_r(t), \tag{21}$$

where $\mathbf{D}_r$ is an identity matrix, implying that $\mathbf{z}_r(t) = \mathbf{x}_r(t)$.

To take an initial step toward the optimal control goal, we seek to estimate the optimal error and energy required to reach the target brain dynamics, and therefore define the following objective: Determine the linear optimal feedback control $\mathbf{u}^*(t)$ such that the system output $\mathbf{z}(t)$ tracks the target dynamics $\mathbf{z}_r(t)$ and minimizes the following stochastic performance index:

$$J = E\left\{\frac{1}{2}\int_{t_0}^{t_f}\left\{\left[\mathbf{z}(t) - \mathbf{z}_r(t)\right]^{\mathrm{T}}\mathbf{Q}\left[\mathbf{z}(t) - \mathbf{z}_r(t)\right] + \mathbf{u}^{\mathrm{T}}(t)\mathbf{R}\mathbf{u}(t),\right\}\mathrm{d}t\right\} \tag{22}$$

where the final time t_f is fixed, and **Q** and **R** are symmetric non-negative definite and symmetric positive definite matrices, respectively.

For this stochastic output feedback tracking system problem, if the system {**A**, **D**} is completely observable and the target model {$\mathbf{A}_r$, $\mathbf{D}_r$} is completely observable, then the optimal control is:

$$\mathbf{u}^*(t) = -\mathbf{K}_1(t)\mathbf{x}(t) + \mathbf{K}_2(t)\mathbf{x}_r(t), \tag{23}$$

where

$$\mathbf{K}_1(t) = \mathbf{R}^{-1}\mathbf{G}^{\mathrm{T}}\mathbf{P}_{11}(t), \tag{24}$$

$$\mathbf{K}_2(t) = -\mathbf{R}^{-1}\mathbf{G}^{\mathrm{T}}\mathbf{P}_{12}(t), \tag{25}$$

where $\mathbf{P}_{11}(t)$ and $\mathbf{P}_{12}(t)$ satisfy the following matrix differential equations and their boundary conditions:

$$-\dot{\mathbf{P}}_{11}(t) = \mathbf{P}_{11}(t)\mathbf{A} + \mathbf{A}^{\mathrm{T}}\mathbf{P}_{11}(t) - \mathbf{P}_{11}(t)\mathbf{B}\mathbf{R}^{-1}\mathbf{B}^{\mathrm{T}}\mathbf{P}_{11}(t) + \mathbf{D}^{\mathrm{T}}\mathbf{Q}\mathbf{D}, \tag{26}$$

$$\mathbf{P}_{11}(t_f) = \mathbf{0}, \tag{27}$$

$$-\dot{\mathbf{P}}_{12}(t) = \mathbf{P}_{12}(t)\mathbf{A}_r + \mathbf{A}^{\mathrm{T}}\mathbf{P}_{12}(t) - \mathbf{P}_{11}(t)\mathbf{B}\mathbf{R}^{-1}\mathbf{B}^{\mathrm{T}}\mathbf{P}_{12}(t) - \mathbf{D}^{\mathrm{T}}\mathbf{Q}\mathbf{D}_r, \tag{28}$$

$$\mathbf{P}_{12}(t_f) = \mathbf{0}. \tag{29}$$

The proof and details[85] can be seen in Supplementary Note 1.

Evaluation of control efficacy. Here, we introduce several definitions, where KL divergence and optimal control energy are employed to assess control effect, while average controllability and modal controllability are used to quantify the intrinsic controllability of brain network systems.

Definition 1. (Kullback-Leibler (KL) divergence[86]). Given two discrete probability distributions P and Q defined on the same probability space, the KL divergence from Q to P is defined as:

$$D_{\mathrm{KL}}(P \parallel Q) = \sum_{x\in\mathcal{X}} P(x)\log\left(\frac{P(x)}{Q(x)}\right), \tag{30}$$

where $\mathcal{X}$ denotes the sample space.

For continuous probability distributions with probability density functions p and q, the KL divergence is given by:

$$D_{\mathrm{KL}}(P \parallel Q) = \int_{-\infty}^{\infty} p(x)\log\left(\frac{p(x)}{q(x)}\right)dx. \tag{31}$$

The KL divergence[86] quantifies the difference between probability distributions P and Q, making it ideal for comparing the stochastic dynamics of brain networks under control. It is always non-negative and equals zero if and only if P and Q are identical almost everywhere. However, it is important to note that KL divergence is not a true metric, as it is not symmetric—i.e., $D_{\mathrm{KL}}(P \parallel Q) \neq D_{\mathrm{KL}}(Q\|P)$—and it does not satisfy the triangle inequality. Unlike deterministic metrics such as Euclidean distance, KL divergence captures the statistical properties (e.g., mean, variance) of noisy fMRI time-series data, aligning with the goal of synchronizing pathological dynamics with healthy target dynamics. Its non-negativity and asymmetry suit the clinical objective of minimizing deviations from healthy baselines, while its robustness to noise ensures reliable evaluation of control performance. By measuring information loss between distributions, KL divergence provides a principled way to assess how well optimal stochastic tracking control improves brain network states toward desired healthy patterns.

Definition 2. (Optimal control energy). The control energy $E_{u_i^*}$ of each control node can be estimated:

$$E_{u_i^*} = \sum_{t=0}^{T-1}(u_i^*(t))^2, \tag{32}$$

where T is the time points in the control horizon.

In the context of optimal stochastic tracking control, we employed a time step of 1 s and 1000 time points for the simulation and calculation of control energy to approximate the resolution used in fMRI sampling. In optimal state transfer control, we similarly used 1000 time points but with a time step of 0.001 s to define the control horizon, as this optimal control method is not suitable for a broad horizon. Consequently, the magnitudes of control energy obtained from the two methods cannot be directly compared, and only their spatial distributions can be produced for correlation analysis.

It is noteworthy that optimal state transfer control aims to drive one brain state to closely approach another target brain state within a limited short time frame. In contrast, optimal stochastic tracking control aims to track an entire brain dynamics towards another target brain dynamics. This highlights the advantage of optimal stochastic tracking control not only in considering the neuronal noise, but also in achieving its intended goal and aligns with the long-term rehabilitation objectives for conditions such as stroke and aphasia.

We quantified the relationship between control energy and the intrinsic controllability of brain network systems. The two types of controllability[43] include:

Definition 3. (Average controllability[43]). Average controllability measures the ease by which input at that node can steer the system into many easily-reachable states, which can be formulated as follows:

$$\mathscr{A}_i(\boldsymbol{A}) = \sqrt{trace\left(\boldsymbol{B}_i^{\top}\left(\int_0^{+\infty}\exp(\boldsymbol{A}t^2 + 2\boldsymbol{A}^{\top}t)dt\right)\boldsymbol{B}_i\right)}, \tag{33}$$

where $\boldsymbol{B}_i$ is a one-dimensional input vector that indicates the i-th node is controlled.

Definition 4. (Modal controllability[43]). Modal controllability reflects the ease of a node to push the brain network system into states that is difficult to reach. It can be defined as:

$$\mathscr{M}_i(\boldsymbol{A}) = \sum_{j=1}^{N}(1 - \lambda_j{}^2(\mathbf{A}))v_{ij}^2, \tag{34}$$

where v_{ij} is elements in the eigenvector of $\boldsymbol{A}$, and λ_j is the j-th eigenvalue.

Related work – Optimal state transfer control for brain network dynamics

For optimal stochastic tracking control, the target dynamics is represented by the average of the approximate dynamics (i.e., the average of the matrix $\mathbf{A}$ and $\mathbf{\Sigma}$) of each healthy participant, and the original dynamics correspond to the approximate dynamics of individual stroke and aphasia patients. For optimal state transfer control, since the state represents a state of a specific moment in time, we employed a clustering method for state selection, following previous research[46].

Target brain states of healthy participants. To define the brain states of healthy participants as target brain states, we referenced the selection method for brain states described in ref. 46. Initially, we detected the peaks of the root mean square (RMS) of whole-brain activity amplitude (N = 100 or 400 regions/nodes defined by Schaefer2018 parcellation). We defined a peak as a frame where the RMS exceeds the values of the preceding and following frames. Subsequently, we aggregated the

corresponding patterns from participants and calculated the Lin's concordance among all patterns. We then applied a variant of modularity maximization to cluster the *Npeak* × *Npeak* matrix, which resulted in 10 clusters. Most clusters were relatively small and/or contained peaks from only a few participants. We defined a brain state as the cluster center that represents peak activations from at least 50% of the participants. Ultimately, we identified four distinct brain states for healthy participants. This approach clusters BOLD time series into recurrent states and is similar to established methods for extracting co-activation patterns (CAPs) from BOLD data.

Original brain states of stroke and post-stroke aphasia patients. To define the brain states of patients as original brain states, and to ensure precision and alignment with personalized treatment applications, we calculated an individual brain state for each stroke and aphasia patient. We selected the peaks of the root mean square (RMS) of whole-brain activity amplitude as the brain state, specifically utilizing the z-scored mean of resting-state fMRI (rs-fMRI) signal amplitudes over time for each brain region[87].

For the traditional optimal brain network control in which the target is to approach the original state to a targeted state (refer to as optimal state transfer control), given the linear deterministic model:

$$\dot{\mathbf{x}}(t) = \mathbf{A}\mathbf{x}(t) + \mathbf{B}\mathbf{u}(t), \tag{35}$$

the cost function is:

$$\min_{\mathbf{u}} \int_0^T \left((\mathbf{x}_T - \mathbf{x}(t))^\top \mathbf{S}(\mathbf{x}_T - \mathbf{x}(t)) + \rho \mathbf{u}(t)^\top \mathbf{u}(t)\right) dt, \tag{36}$$

subject to

$$\dot{\mathbf{x}}(t) = \mathbf{A}\mathbf{x}(t) + \mathbf{B}\mathbf{u}(t), \tag{37}$$

$$\mathbf{x}(0) = \mathbf{x}_0, \tag{38}$$

$$\mathbf{x}(T) = \mathbf{x}_T. \tag{39}$$

The optimal input can be estimated as follows:

$$\mathbf{u}_k^* = -\frac{1}{2\rho}\mathbf{B}^\top \mathbf{p}^*, \tag{40}$$

$$\dot{\mathbf{x}}^* = \mathbf{A}\mathbf{x}^* - \frac{1}{2\rho}\mathbf{B}\mathbf{B}^\top \mathbf{p}^*, \tag{41}$$

where $\mathbf{u}_k^*$ can be obtained through solving corresponding differential equations. The proof and details[44] can be seen in Supplementary Note 2.

Statistics and reproducibility

We performed statistical analyses using three primary methods. First, we compared FC between groups using the Kruskal-Wallis test, with FDR correction for multiple comparisons. Second, we used paired *t*-tests to evaluate the control effect by comparing the KL divergence of both the controlled and uncontrolled dynamics against the target dynamics. Finally, we performed correlation analyses (reporting Pearson's *R* values and *p* values) to examine the relationships between tracking energy, average controllability, and modal controllability, as well as between optimal transfer control energy and other metrics. The same correlation methodology was applied to all analyses in the Supplementary Files. The sample sizes for each group are: Anomic = 46, Broca = 65, Conduction = 23, Global = 14, Normal Stroke = 26, Healthy = 36. All variables were carefully examined for outliers, data entry errors, and missing values. Sex and gender were considered as potential factors that could influence the results. We employed a regression-out approach (one of the most used harmonization techniques for pre-processed data to eliminate any potential factors that could influence the results, including sites, equipment, acquisition parameters, and the age and sex or gender of individuals. To assess the reproducibility and robustness of our findings, we conducted primary analyses using alternative parcellations with 100 and 400 cortical regions, and confirmed that the results remained consistent.

Reporting summary

Further information on research design is available in the Nature Portfolio Reporting Summary linked to this article.

Conclusion

In this paper, we have extended the existing optimal state transfer control of brain networks to optimal stochastic tracking control, which is more aligned with the objectives of brain stimulation. The results indicate that the energy of stochastic tracking control is significantly negatively correlated with the average controllability of the brain network system, whereas the energy of optimal state transfer control is related to the selected target state. Stochastic tracking control of brain networks represents an important direction for future research in brain network control, guiding stimulation paradigms towards minimal cost and optimal therapeutic effect.

Data availability

Raw data of the post-stroke aphasia is publicly available at OpenNeuro (https://doi.org/10.18112/openneuro.ds004884.v1.0.1)[88]. Raw data of the healthy participants is publicly available at OpenNeuro (https://doi.org/10.18112/openneuro.ds003871.v1.0.2)[89]. Raw data for generating figures in this paper is available at Figshare (https://doi.org/10.6084/m9.figshare.30434584.v2)[90].

Code availability

The network model parameter estimation codes are available at Github (https://github.com/mb-BCA/pyMOU/tree/master). The optimal control codes are available at Github (https://github.com/Kangli-Dong).

Received: 14 February 2025; Accepted: 5 November 2025;
Published online: 13 December 2025

References

1. Baggio, H.-C. et al. Functional brain networks and cognitive deficits in parkinson's disease. *Hum. Brain Mapp.* **35**, 4620–4634 (2014).
2. Kim, J. et al. Abnormal intrinsic brain functional network dynamics in parkinson's disease. *Brain* **140**, 2955–2967 (2017).
3. Dennis, E. L. & Thompson, P. M. Functional brain connectivity using fMRI in aging and alzheimer's disease. *Neuropsychol. Rev.* **24**, 49–62 (2014).
4. DelEtoile, J. & Adeli, H. Graph theory and brain connectivity in alzheimer's disease. *Neuroscientist* **23**, 616–626 (2017).
5. Ashtiani, S. N. M. et al. Altered topological properties of brain networks in the early MS patients revealed by cognitive task-related fMRI and graph theory. *Biomed. Signal Process. Control* **40**, 385–395 (2018).
6. Farahani, F. V., Karwowski, W. & Lighthall, N. R. Application of graph theory for identifying connectivity patterns in human brain networks: a systematic review. *Front. Neurosci.* **13**, 585 (2019).
7. Agosta, F. et al. Disrupted brain connectome in semantic variant of primary progressive aphasia. *Neurobiol. Aging* **35**, 2646–2655 (2014).
8. Tao, Y., Ficek, B., Rapp, B. & Tsapkini, K. Different patterns of functional network reorganization across the variants of primary progressive aphasia: a graph-theoretic analysis. *Neurobiol. aging* **96**, 184–196 (2020).
9. Chen, X. et al. Disrupted brain connectivity networks in aphasia revealed by resting-state fMRI. *Front. Aging Neurosci.* **13**, 666301 (2021).

10. Hallett, M. Transcranial magnetic stimulation: a primer. *Neuron* **55**, 187–199 (2007).
11. Feng, W., Bowden, M. G. & Kautz, S. Review of transcranial direct current stimulation in poststroke recovery. *Top Stroke rehabilitation* **20**, 68–77 (2013).
12. Polanía, R., Nitsche, M. A. & Ruff, C. C. Studying and modifying brain function with non-invasive brain stimulation. *Nat. Neurosci.* **21**, 174–187 (2018).
13. Greene, A. S., Horien, C., Barson, D., Scheinost, D. & Constable, R. T. Why is everyone talking about brain state? *Trends Neurosci.* **46**, 508–524 (2023).
14. Karrer, T. M. et al. A practical guide to methodological considerations in the controllability of structural brain networks. *J. neural Eng.* **17**, 026031 (2020).
15. Cornblath, E. J. et al. Temporal sequences of brain activity at rest are constrained by white matter structure and modulated by cognitive demands. *Commun. Biol.* **3**, 261 (2020).
16. Parkes, L. et al. Asymmetric signaling across the hierarchy of cytoarchitecture within the human connectome. *Sci. Adv.* **8**, eadd2185 (2022).
17. Sun, H. et al. Network controllability of structural connectomes in the neonatal brain. *Nat. Commun.* **14**, 5820 (2023).
18. Stiso, J. et al. White matter network architecture guides direct electrical stimulation through optimal state transitions. *Cell Rep.* **28**, 2554–2566 (2019).
19. Cooper, R. A., Kurkela, K. A., Davis, S. W. & Ritchey, M. Mapping the organization and dynamics of the posterior medial network during movie watching. *NeuroImage* **236**, 118075 (2021).
20. Braun, U. et al. Brain network dynamics during working memory are modulated by dopamine and diminished in schizophrenia. *Nat. Commun.* **12**, 3478 (2021).
21. Parkes, L. et al. Network controllability in transmodal cortex predicts positive psychosis spectrum symptoms. *Biol. Psychiatry* **90**, 409–418 (2021).
22. Mahadevan, A. S. et al. Alprazolam modulates persistence energy during emotion processing in first-degree relatives of individuals with schizophrenia: a network control study. *Mol. psychiatry* **28**, 3314–3323 (2023).
23. Singleton, S. P. et al. Receptor-informed network control theory links lsd and psilocybin to a flattening of the brain's control energy landscape. *Nat. Commun.* **13**, 5812 (2022).
24. Singleton, S. P. et al. Network control energy reductions under DMT relate to serotonin receptors, signal diversity, and subjective experience. *Commun. Biol.* **8**, 631 (2025).
25. Bernhardt, J. et al. Agreed definitions and a shared vision for new standards in stroke recovery research: the stroke recovery and rehabilitation roundtable taskforce. *Int. J. Stroke* **12**, 444–450 (2017).
26. Varkanitsa, M. & Kiran, S. Insights gained over 60 years on factors shaping post-stroke aphasia recovery: A commentary on vignolo (1964). *Cortex* **170**, 90–100 (2024).
27. Sheppard, S. M. & Sebastian, R. Diagnosing and managing post-stroke aphasia. *Expert Rev. Neurotherapeutics* **21**, 221–234 (2021).
28. Wade, D., Hewer, R. L., David, R. M. & Enderby, P. M. Aphasia after stroke: natural history and associated deficits. *J. Neurol., Neurosurg. Psychiatry* **49**, 11–16 (1986).
29. Adeyemo, B. O., Simis, M., Macea, D. D. & Fregni, F. Systematic review of parameters of stimulation, clinical trial design characteristics, and motor outcomes in non-invasive brain stimulation in stroke. *Front. psychiatry* **3**, 88 (2012).
30. Breining, B. L. & Sebastian, R. Neuromodulation in post-stroke aphasia treatment. *Curr. Phys. Med. Rehabilitation Rep.* **8**, 44–56 (2020).
31. Honey, C. J. et al. Predicting human resting-state functional connectivity from structural connectivity. *Proc. Natl Acad. Sci.* **106**, 2035–2040 (2009).
32. Kucyi, A. & Davis, K. D. The dynamic pain connectome. *Trends Neurosci.* **38**, 86–95 (2015).
33. Jirsa, V. K., Stacey, W. C., Quilichini, P. P., Ivanov, A. I. & Bernard, C. On the nature of seizure dynamics. *Brain* **137**, 2210–2230 (2014).
34. Wardlaw, J. M., Smith, C. & Dichgans, M. Small vessel disease: mechanisms and clinical implications. *Lancet Neurol.* **18**, 684–696 (2019).
35. Menon, V., Palaniyappan, L. & Supekar, K. Integrative brain network and salience models of psychopathology and cognitive dysfunction in schizophrenia. *Biol. psychiatry* **94**, 108–120 (2023).
36. Desowska, A. & Turner, D. L. Dynamics of brain connectivity after stroke. *Rev. Neurosci.* **30**, 605–623 (2019).
37. Rabinovich, M. I., Friston, K. J. & Varona, P.*Principles of brain dynamics: global state interactions* (2023).
38. Liu, J. et al. Progress of brain network studies on anesthesia and consciousness: framework and clinical applications. *Engineering* **20**, 77–95 (2023).
39. Schaefer, A. et al. Local-global parcellation of the human cerebral cortex from intrinsic functional connectivity MRI. *Cereb. Cortex* **28**, 3095–3114 (2018).
40. Siegel, J. S. et al. Disruptions of network connectivity predict impairment in multiple behavioral domains after stroke. *Proc. Natl Acad. Sci.* **113**, E4367–E4376 (2016).
41. Baldassarre, A., Ramsey, L. E., Siegel, J. S., Shulman, G. L. & Corbetta, M. Brain connectivity and neurological disorders after stroke. *Curr. Opin. Neurol.* **29**, 706–713 (2016).
42. Park, C.-H et al. Longitudinal changes of resting-state functional connectivity during motor recovery after stroke. *Stroke* **42**, 1357–1362 (2011).
43. Gu, S. et al. Controllability of structural brain networks. *Nat. Commun.* **6**, 8414 (2015).
44. Gu, S. et al. Optimal trajectories of brain state transitions. *NeuroImage* **148**, 305–317 (2017).
45. Wilmskoetter, J. et al. Language recovery after brain injury: a structural network control theory study. *J. Neurosci.* **42**, 657–669 (2022).
46. Betzel, R. F. et al. Controlling the human connectome with spatially diffuse input signals. *bioRxiv* 2024–02 (2024).
47. Fang, F. et al. Personalizing repetitive transcranial magnetic stimulation for precision depression treatment based on functional brain network controllability and optimal control analysis. *NeuroImage* **260**, 119465 (2022).
48. Stagg, C. J. & Nitsche, M. A. Physiological basis of transcranial direct current stimulation. *Neuroscientist* **17**, 37–53 (2011).
49. Roth, B. L. Dreadds for neuroscientists. *Neuron* **89**, 683–694 (2016).
50. Boyden, E. S., Zhang, F., Bamberg, E., Nagel, G. & Deisseroth, K. Millisecond-timescale, genetically targeted optical control of neural activity. *Nat. Neurosci.* **8**, 1263–1268 (2005).
51. Jacobson, G. A. et al. Subthreshold voltage noise of rat neocortical pyramidal neurones. *J. Physiol.* **564**, 145–160 (2005).
52. Kamiya, S., Kawakita, G., Sasai, S., Kitazono, J. & Oizumi, M. Optimal control costs of brain state transitions in linear stochastic systems. *J. Neurosci.* **43**, 270–281 (2023).
53. Breakspear, M. Dynamic models of large-scale brain activity. *Nat. Neurosci.* **20**, 340–352 (2017).
54. Kurtin, D. L. et al. Moving from phenomenological to predictive modelling: Progress and pitfalls of modelling brain stimulation in-silico. *Neuroimage* **272**, 120042 (2023).
55. Perl, Y. S. et al. Model-based whole-brain perturbational landscape of neurodegenerative diseases. *Elife* **12**, e83970 (2023).
56. Deco, G. et al. Awakening: Predicting external stimulation to force transitions between different brain states. *Proc. Natl Acad. Sci.* **116**, 18088–18097 (2019).

57. Vohryzek, J. et al. Dynamic sensitivity analysis: Defining personalised strategies to drive brain state transitions via whole brain modelling. *Computational Struct. Biotechnol. J.* **21**, 335–345 (2023).
58. Vohryzek, J. et al. Brain dynamics predictive of response to psilocybin for treatment-resistant depression. *Brain Commun.* **6**, fcae049 (2024).
59. Tzourio-Mazoyer, N. et al. Automated anatomical labeling of activations in spm using a macroscopic anatomical parcellation of the mni mri single-subject brain. *Neuroimage* **15**, 273–289 (2002).
60. Yeo, B. T. et al. The organization of the human cerebral cortex estimated by intrinsic functional connectivity. *J. Neurophysiol.* **106**, 1125–1165 (2011).
61. Desikan, R. S. et al. An automated labeling system for subdividing the human cerebral cortex on mri scans into gyral based regions of interest. *Neuroimage* **31**, 968–980 (2006).
62. Deng, Z.-D., Lisanby, S. H. & Peterchev, A. V. Electric field depth–focality tradeoff in transcranial magnetic stimulation: simulation comparison of 50 coil designs. *Brain stimulation* **6**, 1–13 (2013).
63. Parkes, L. et al. A network control theory pipeline for studying the dynamics of the structural connectome. *Nat. Protoc.* **19**, 3721–3749 (2024).
64. Sun, J. & Motter, A. E. Controllability transition and nonlocality in network control. *Phys. Rev. Lett.* **110**, 208701 (2013).
65. Manjunatha, K. K. H. et al. Controlling target brain regions by optimal selection of input nodes. *PLOS Computational Biol.* **20**, e1011274 (2024).
66. Ruohonen, J. & Karhu, J. Navigated transcranial magnetic stimulation. *Neurophysiologie Clin./Clin. Neurophysiol.* **40**, 7–17 (2010).
67. Ferbert, A. et al. Interhemispheric inhibition of the human motor cortex. *J. Physiol.* **453**, 525–546 (1992).
68. Roth, Y., Levkovitz, Y., Pell, G. S., Ankry, M. & Zangen, A. Safety and characterization of a novel multi-channel TMS stimulator. *Brain Stimulation* **7**, 194–205 (2014).
69. Momi, D. et al. Cognitive enhancement via network-targeted cortico-cortical associative brain stimulation. *Cereb. Cortex* **30**, 1516–1527 (2020).
70. Chen, T., Liu, X. & Lu, W. Pinning complex networks by a single controller. *IEEE Trans. Circuits Syst. I: Regul. Pap.* **54**, 1317–1326 (2007).
71. Vega, C. J. et al. Trajectory tracking on complex networks via inverse optimal pinning control. *IEEE Trans. Autom. Control* **64**, 767–774 (2018).
72. Fridriksson, J. et al. Revealing the dual streams of speech processing. *Proc. Natl Acad. Sci.* **113**, 15108–15113 (2016).
73. Fridriksson, J. et al. Anatomy of aphasia revisited. *Brain* **141**, 848–862 (2018).
74. Gibson, M. et al. The aphasia recovery cohort, an open-source chronic stroke repository. *Sci. Data* **11**, 981 (2024).
75. Wahlheim, C. N., Christensen, A. P., Reagh, Z. M. & Cassidy, B. S. Intrinsic functional connectivity in the default mode network predicts mnemonic discrimination: A connectome-based modeling approach. *Hippocampus* **32**, 21–37 (2022).
76. Whitfield-Gabrieli, S. & Nieto-Castanon, A. Conn: a functional connectivity toolbox for correlated and anticorrelated brain networks. *Brain Connectivity* **2**, 125–141 (2012).
77. Power, J. D. et al. Functional network organization of the human brain. *Neuron* **72**, 665–678 (2011).
78. Gordon, E. M. et al. Generation and evaluation of a cortical area parcellation from resting-state correlations. *Cereb. Cortex* **26**, 288–303 (2016).
79. Fan, L. et al. The human brainnetome atlas: a new brain atlas based on connectional architecture. *Cereb. Cortex* **26**, 3508–3526 (2016).
80. Gallo, S. et al. Functional connectivity signatures of major depressive disorder: machine learning analysis of two multicenter neuroimaging studies. *Mol. Psychiatry* **28**, 3013–3022 (2023).
81. Wang, Y.-W., Chen, X. & Yan, C.-G. Comprehensive evaluation of harmonization on functional brain imaging for multisite data-fusion. *NeuroImage* **274**, 120089 (2023).
82. Timme, M. & Casadiego, J. Revealing networks from dynamics: an introduction. *J. Phys. A: Math. Theor.* **47**, 343001 (2014).
83. Gilson, M., Moreno-Bote, R., Ponce-Alvarez, A., Ritter, P. & Deco, G. Estimation of directed effective connectivity from fmri functional connectivity hints at asymmetries of cortical connectome. *PLoS Comput. Biol.* **12**, e1004762 (2016).
84. Gilson, M. et al. Model-based whole-brain effective connectivity to study distributed cognition in health and disease. *Netw. Neurosci.* **4**, 338–373 (2020).
85. Lewis, F. L., Vrabie, D. L. & Syrmos, V. L. Optimal control. *Wiley Online Library* (2012).
86. Kullback, S. & Leibler, R. A. On information and sufficiency. *Ann. Math. Stat*. **22**, 79–86 (1951).
87. Weaver, K. E. et al. Directional patterns of cross frequency phase and amplitude coupling within the resting state mimic patterns of fMRI functional connectivity. *Neuroimage* **128**, 238–251 (2016).
88. Gibson, M. et al. “aphasia recovery cohort (arc) dataset" (2023).
89. Wahlheim, C. N., Christensen, A. P., Cassidy, B. S. & Reagh, Z. M. “resting-state for 34 younger and 28 older adults" (2021).
90. Dong, K. A New Perspective on Brain Stimulation Interventions through Optimal Stochastic Tracking Control for Brain Network Dynamics [dataset] https://figshare.com/articles/dataset/optimal_tracking_control_paper_files/30434584 (2025).

Acknowledgements

This work was supported by Guangdong Basic and Applied Basic Research Foundation of China (2025A1515012149), National Key R&D Plan (2025YFC3410002) of China, National Natural Science Foundation of China (82172056), Zhejiang Provincial Natural Science Foundation of China (LR23F010003), National Key R&D Program of China (2022ZD0117902), Key R&D Program of Zhejiang Province (2024C04032), and STU Scientific Research Initiation (NTF24004T).

Author contributions

K.D. and S.C.: conceptualization, methodology, investigation, result visualization and writing-original draft; K.D., S.C. and Y.D.: investigation and result visualization; K.D., S.C. and L.Z.: methodology and writing-review and editing; X.L., W.L. and Y.Z.: writing-review and editing; K.D. and Y.S.: supervision and writing-review.

Competing interests

The authors declare no competing interests.

Additional information

Supplementary information The online version contains supplementary material available at https://doi.org/10.1038/s42003-025-09184-4.

Correspondence and requests for materials should be addressed to Siya Chen.

Peer review information *Communications Biology* thanks Zhenhu Liang and the other, anonymous, reviewer(s) for their contribution to the peer review of this work. Primary Handling Editor: Jasmine Pan. A peer review file is available.